# Magnetic field induced reentrance of superconductivity in the cage-type superconductor $Y_5Rh_6Sn_{18}$

M. Fijałkowski [1,2] M. M. Maśka [3] J. Deniszczyk [4] and A. Ślebarski [5,*]

[1]*Institute of Physics, University of Silesia in Katowice, 75 Pułku Piechoty 1, 41-500 Chorzów, Poland*
[2]*Centre for Advanced Materials and Smart Structures, Polish Academy of Sciences, Okólna 2, 50-950 Wrocław, Poland*
[3]*Department of Theoretical Physics, Wroclaw University of Science and Technology, Wybrzeże Wyspiańskiego 27, 50-370 Wrocław, Poland*
[4]*Institute of Materials Engineering, University of Silesia in Katowice, 75 Pułku Piechoty 1A, 41-500 Chorzów, Poland*
[5]*Institute of Low Temperature and Structure Research, Polish Academy of Sciences, P. O. Box 1410, 50-950 Wrocław, Poland*

(Received 27 August 2021; revised 6 October 2021; accepted 12 October 2021; published 25 October 2021)

The morphological and/or chemical disorder is commonly known as detrimental to superconductivity and typically reduces the critical temperature $T_c$. We present research on the skutterudite-related $Y_5Rh_6Sn_{18}$ system, where local atomic disorder leads to novel disorder-enhanced superconductivity. Our present studies focus on the series of $Y_{4.5}M_{0.5}Rh_6Sn_{18}$ compounds, where the metallic dopants $M$ = Ca, Ti, Sr, Zr, La, or Lu, when they are smaller than the atomic radius of Y (the case of Ti, Zr, Lu, or vacancies at the Y sites), generate the so-called *peak effect* at $T < T_c$ in the fields smaller than the critical field $H_{c2}$. The peak effect is well documented experimentally by measurements of the temperature variations in electric transport and ac magnetic susceptibility under external magnetic fields. In accordance with the commonly accepted explanation of the peak effect, we assume that the magnetic field induced reentrance of superconductivity in $Y_{4.5}M_{0.5}Rh_6Sn_{18}$ results from a change in the structure of the vortex lattice close to $H_{c2}$. Using a simple theoretical model we argue that the effectiveness of this mechanism can depend on the size of the dopant. We also investigate the band structure properties by x-ray electron spectroscopy and *ab initio* calculations. It seems interesting that the density functional theory predicts a magnetic moment on the dopant Ti, which is a reason for the Kondo effect, confirmed experimentally.

DOI: 10.1103/PhysRevB.104.165306

## I. INTRODUCTION

In the conventional superconducting (SC) systems, disorder, which can be morphological or chemical, is unwanted since superconductivity is suppressed and even disappears as disorder increases. Moreover, the effect of the disorder on superconductivity (most often it is a local disorder) depends on whether the dopant is magnetic or not and the dimensionality of the superconducting system. The appearance of disorder is commonly known as detrimental to two-dimensional (2D) superconductivity, and typically results in decreasing of the critical transition temperature $T_c$ [1–3]. For 3D superconducting systems, if the disorder is *magnetic*, a systematic suppression of $T_c$ is manifested for any pairing symmetry as disorder increases, according to the relationship first calculated by Abrikosov and Gor'kov [4,5]. Conversely, according to Anderson's theorem [6] an *s*-wave superconductor should be robust against nonmagnetic disorder due to the ability of the quasiparticle states to form time-reversed pairs, though several theoretical calculations of the possible decreasing in $T_c$ have also been presented for nonmagnetic scatterers in multiband superconductors with generalized *s*-wave order [7]. In the case of strongly correlated electron systems (SCESs), atomic disorder, acting as a perturbation within the critical regime, can lead to novel phenomena such as the disorder-enhanced superconductivity. If the disorder is inhomogeneous on the length scale similar to the coherence length $\xi$, then it is possible to observed an enhancement of the superconducting transition temperature, e.g., in SCES superconducting $PrOs_4Sb_{12}$ [8–12], $CeIrIn_5$ [13], $CePt_3Si$ [14], high-temperature $Bi_2Sr_2CaCu_2O_{8+x}$ superconductors [15,16], or superconducting topological SnSb [17]. An anomalous enhancement of superconductivity induced by structural defects is also possible to be observed in 2D superconducting systems; in particular the disorder-enhanced superconductivity emerges in $TaS_2$ monolayers doped with the hydrion ($H^+$) [18].

Our present studies are focused on skutterudite-related superconductors for which we have documented a similar enhancement of $T_c$ caused by a disorder (the research has been summarized in a review article [19]). The disorder-generated enhancement in $T_c$ is well explained theoretically by the Gastiasoro and Andersen model [20], both at the small and large limit of disorder present in these SCES superconductors. The various literature data and our recently published results allowed us to interpret the appearance of the *high-temperature* $T_c^\star$ superconducting phase as a result of the local atomic disorder and/or an inhomogeneous doping effect. We have proposed a phenomenological model that explains the relationships $T_c^\star > T_c$ and $|\frac{dT_c^\star}{dP}| > |\frac{dT_c}{dP}|$ due to the greater lattice stiffening of the $T_c^\star$ phase, as well as the relation $\Gamma_G^\star > \Gamma_G$ ($\Gamma_G \sim B_m$, where $B_m$ is the bulk modulus) between the Grüneisen parameters characterizing the respective phases [19].

In this study we report the observation of the *peak effect* (PE) in the series of disordered $Y_{4.5}M_{0.5}Rh_6Sn_{18}$ polycrys-

*Author to whom correspondence should be addressed: andrzej.slebarski@us.edu.pl

 

talline samples; for all of them the coexistence of the bulk ($T_c$) and *high-temperature* ($T_c^\star$) superconducting phases is experimentally documented. The PE phenomenon relates to an anomalous increase in the critical current density ($J_c$) in type-II superconductors with increasing temperature, or magnetic field, in a narrow range below the upper critical field $H_{c2}(T)$ [21]. This PE phenomenon was found in a large variety of conventional superconductors, such as Nb [22], $V_3Si$ [23], $CeRu_2$ [24], $Yb_3Rh_4Sn_{13}$ [25], and $Ca_3Rh_4Sn_{13}$ [26] quasiskutterudites, the $UPd_2Al_3$ heavy-fermion superconductor [27,28], and the $YBa_2Cu_3O_7$ high-temperature superconductor [29,30]. Over the years, understanding PE has been one of the most challenging tasks in the physics of vortex-lattice pinning. Two different mechanisms have been considered to explain the PE phenomenon. A classical scenario [31] attempts to relate PE to a faster rate of decrease in the elastic modulus of the flux-line lattice with an increase in temperature as compared to that of the elementary pinning force. A second scenario [28] considers the PE in heavy-fermion superconductors, which could be caused as a first-order transition by the realization of a generalized Fulde-Ferrell-Larkin-Ovchinnikov state at high fields and low temperatures, lower than $0.55T_c(0)$ [32,33]; however, this scenario seems to be inappropriate to interpret PE behavior in the superconductors studied here. In this paper we investigate the electrical transport, thermodynamic properties, and the electronic structure of the series of the $Y_{4.5}M_{0.5}Rh_6Sn_{18}$ superconductors, focusing on the PE and various interesting features associated with it. Based on our present results and other relevant experimental information from our previous observations and the existing literature data, we also discuss the nature of the PE in the $Y_5Rh_6Sn_{18}$ superconductor doped with metal $M$.

The critical behavior at $T_c$ is discussed here as a result of two effects. The first is the peak effect, which is not an enhancement of the thermodynamic superconducting critical temperature, but mainly an enhancement of the critical current. The second is an inhomogeneous $T_c^\star$ SC phase due to doping, that would appear to be closer to a pressure effect and enhancement of its superconductivity with increasing of the local inhomogeneity. However, both are strongly related to local inhomogeneities due to atomic disorder.

## II. EXPERIMENTAL AND COMPUTATIONAL DETAILS

The $Y_{4.5}M_{0.5}Rh_6Sn_{18}$ polycrystalline samples were prepared by the arc-melting technique and then annealed at 870 °C for 2 weeks. All samples were examined by x-ray diffraction (XRD) analysis and found to have a tetragonal structure (space group $I4_1/acd$) [34,35]. Patterns of samples were collected on a PANalytical Empyrean diffractometer equipped with a Cu $K\alpha_{1,2}$ a source. Diffractograms were refined using the FullProf Suite set of programs [36]. Stoichiometry and homogeneity were checked by the electron microprobe technique (scanning microscope JSM-5410).

The x-ray photoelectron spectroscopy (XPS) spectra were obtained with monochromatized Al $K_\alpha$ radiation at room temperature in a vacuum of $6 \times 10^{-10}$ Torr using a PHI 5700 ESCA spectrometer. The samples were broken under a high vacuum immediately before measuring the spectra.

The electronic band structure was calculated using the full-potential linearized augmented plane wave (FP-LAPW) method complemented with local orbitals (LOs) [37] implemented in the WIEN2k computer code [38]. The core states were treated within the fully relativistic density functional formalism while for the valence and semicore states the scalar-relativistic Kohn-Sham approach was applied with spin-orbit coupling accounted for by means of the second variational method [37]. The generalized gradient approximation (GGA) form of the exchange-correlation energy functional, together with the parametrization (PBEsol) derived for solids by Perdew *at al.* [39], was applied. For the correlated Lu $4f$ and Rh $4d$ band states, the exchange correlation potential was corrected by the Hubbard-type correlation interaction applying the LSDA+$U$ method [40] with $U_{\text{eff}}$ equal 6.8 eV and 3.0 eV for the Lu $4f$ and Rh $4d$ states, respectively. The $k$ mesh was tested against the total energy convergence and satisfactory precision of a few meV was achieved with a $7 \times 7 \times 7$ mesh ($N_k = 40\vec{k}$ vectors in the irreducible Brillouin zone). The set of local orbitals and valence states of Ti and Sr atoms was assumed as follows: Ti, $[3s^2 3p^6]_{\text{LO}}(3d^2 4s^2)_{\text{VB}}$; Sr, $[4s^2 4p^6]_{\text{LO}}(5s^2)_{\text{VB}}$. For other details on similarly made computations see, e.g., Refs. [41,42]. The *ab initio* calculations were performed using the experimental lattice parameters (tetragonal structure, space group $I4_1/acd$). To simulate impurities $M$ in the $Y_5Rh_6Sn_{18}$ structure the supercell approach was applied with the supercell spanned by $a(100)$, $b(010)$, and $c(001)$ primitive vectors. The structure with fractional concentration of $M$ ($M$ = Ti, Sr) dopant atoms was prepared by replacing selected Y atoms with $M$ ones. In each case the atomic positions were relaxed using the multisecant rank one algorithm implemented in the WIEN2k code.

## III. THE SYSTEM OF BCS $Y_{4.5}M_{0.5}Rh_6Sn_{18}$ SUPERCONDUCTORS ($M$ = Y, Ca, Ti, Sr, Zr, La, and Lu): RESULTS AND DISCUSSION

### A. $Y_{4.5}M_{0.5}Rh_6Sn_{18}$: Structural properties

The results from refining the XRD data are displayed in Table I. The final least-squares refinement cycle gave the weighted-profile $R$ factor $R_{\text{wp}} < 3\%$ ($R_{\text{wp}} = \{\sum_i w_i[y_i(\text{obs}) - y_i(\text{calc})]^2 / \sum_i w_i y_i(\text{obs})^2\}^{1/2} \times 100\%$, where $y_i$ is a value of observed or calculated intensity, and $w_i$ is the weight [43]) and $R_{\text{Bragg}} < 2\%$. Figure 1 shows representative XRD pattern for $Y_{4.5}Sr_{0.5}Rh_6Sn_{18}$ with Rietveld refinements. The unit cell volume of $Y_{4.5}M_{0.5}Rh_6Sn_{18}$ has a linear scaling with the atomic radius of metal $M$ (as shown in Fig. 2), which suggests that the content of $M$ is similar (of about 0.5 per formula unit) in each component of the series, as expected.

We note that energy-dispersive x-ray spectroscopy measurements indicate a deficiency of Y and similar excess of Sn with a composition close to $Y_{4.1}M_{0.5}Rh_6Sn_{18.5}$. Our band structure calculation carried out for similar off-stoichiometry skutterudite-related compounds justifies their semimetallic nature in the normal state, explicitly visible in the temperature variation of the resistivity $\rho(T)$ for $T > T_c$; this will be discussed later (Sec. III D). Figure 3 displays variation in stoichiometry over the length of the $Y_{4.5}Sr_{0.5}Rh_6Sn_{18}$ sample. The nanoscale inhomogeneity obtained over the length scale

TABLE I. The parameters obtained from structural and microanalysis characterization of $Y_{4.5}M_{0.5}Rh_6Sn_{18}$ superconductors. The energy-dispersive x-ray analysis gives the average Y : $M$ : Rh : Sn stoichiometric ratio for the sample surface, respectively, when the content of Rh is normalized to 6 atoms per formula unit.

| $Y_{4.5}M_{0.5}Rh_6Sn_{18}$ $M$ | Stoichiometry Y : $M$ : Rh : Sn | Lattice parameters (Å) | $V$ (Å$^3$) | $R_{wp}$ (%) |
|---|---|---|---|---|
| Ca | $4.10 \pm 0.11 : 0.60 \pm 0.16 : 6.0 \pm 0.11 : 18.21 \pm 0.12$ | $a = 13.7678(1), c = 27.5430(8)$ | 5220.85(8) | 1.9 |
| Ti | $4.10 \pm 0.10 : 0.37 \pm 0.13 : 6.0 \pm 0.13 : 18.40 \pm 0.16$ | $a = 13.7164(1), c = 27.3207(0)$ | 5140.11(5) | 3.6 |
| Sr | $4.10 \pm 0.25 : 0.50 \pm 0.18 : 6.0 \pm 0.25 : 18.60 \pm 0.30$ | $a = 13.7921(6), c = 27.5825(7)$ | 5246.85(9) | 2.0 |
| Y | $4.60 \pm 0.11 : 6.0 \pm 0.13 : 18.10 \pm 0.15$ | $a = 13.7601(2), c = 27.5412(3)$ | 5214.68(2) | 2.6 |
| Zr | $4.20 \pm 0.17 : 0.57 \pm 0.15 : 6.0 \pm 0.18 : 18.60 \pm 0.23$ | $a = 13.7011(1), c = 27.4891(2)$ | 5160.27(2) | 3.6 |
| La | $4.90 \pm 0.09 : 0.50 \pm 0.07 : 6.0 \pm 0.15 : 18.80 \pm 0.19$ | $a = 13.7319(9), c = 27.3479(7)$ | 5156.94(1) | 4.3 |
| Lu | $4.10 \pm 0.13 : 0.60 \pm 0.13 : 6.0 \pm 0.16 : 18.50 \pm 0.18$ | $a = 13.7542(3), c = 27.5146(1)$ | 5205.18(3) | 3.2 |

similar to coherence length was observed too for the remaining $M$ components of the $Y_{4.1}M_{0.5}Rh_6Sn_{18.5}$ series. This local inhomogeneity, experimentally confirmed as a bulk property of various quasiskutterudites [44], is a reason for the appearance of the *high-temperature inhomogeneous superconducting phase* with critical temperature $T_c^\star > T_c$ [20].

### B. Thermodynamic characterization

The systematic studies of atomic-scale disorder in the skutterudite-related superconducting compounds in the form of local defects and vacancies have received our attention, particularly because of observations of new superconducting phenomena in these materials [44]. Namely, our previous comprehensive investigations have shown that atomic disorder has a significant impact on the increase in $T_c$. Here we documented that the effective increase of disorder by doping with metal $M$ or by vacancies could be a reason for the appearance of the peak effect in the system of $Y_{4.5}M_{0.5}Rh_6Sn_{18}$ superconductors when the dopant $M$ is smaller than Y, or is a vacancy. The most important results from the measured various thermodynamic and electric transport characteristics are summarized in Table II.

Figure 4 compares the ac mass magnetic susceptibility $\chi_{ac}$ measured for the series of $Y_{4.5}M_{0.5}Rh_6Sn_{18}$ compounds at $\nu = 100$ Hz; details are discussed below (see also Table II).

Figure 5 displays the frequency dependence of real ($\chi'$) and imaginary ($\chi''$) components of ac mass magnetic susceptibility $\chi_{ac}$ for $Y_{4.5}Sr_{0.5}Rh_6Sn_{18}$. The susceptibility of the Sr sample was chosen as an example, and the remaining compounds show very similar $\chi_{ac}(T)$ behavior. First, $\chi'$ and $\chi''$ show between ~5.6 K and $T_c^\star$ a broad transition between normal and superconducting states (cf. inset to Fig. 5), which is related to formation of separate inhomogeneous and superconducting regions with strongly enhanced local critical temperatures $T_c$, but they do not form a continuous path across the system. As long as the zero-resistivity islands do not form a continuous path, the sample remains in the normal state, but with decreasing resistivity. Then, $\chi'$ displays a broad transition between normal and superconducting states, which signals the presence of an inhomogeneous *high-temperature* superconducting $T_c^\star$ phase, while $d\chi'/dT$ shows two well-separated maxima at $T_c^\star$ and at $T_c$. Moreover, perfect diamagnetism of the full Meissner state with estimated value of $\chi' = -1/(4\pi d) \approx -0.01$ emu/g and mass

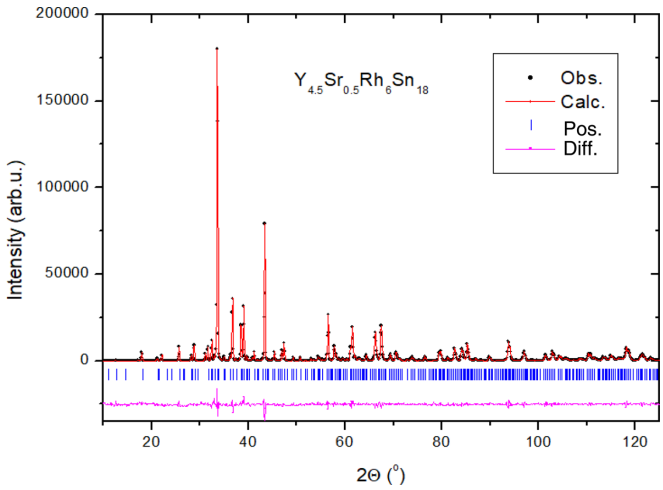


FIG. 1. Plot of Rietveld refinement for $Y_{4.5}Sr_{0.5}Rh_6Sn_{18}$. Black dots, observed pattern; red line, calculated; blue ticks, Bragg peak positions; magenta line, the difference between calculated and experimentally observed XRD patterns.

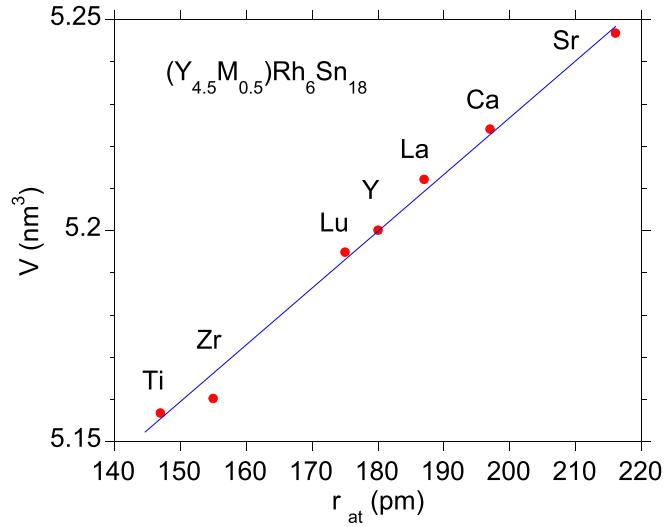


FIG. 2. Cell volumes for the series of the $Y_{4.5}M_{0.5}Rh_6Sn_{18}$ compounds vs atomic radius of metal $M$. The dashed blue line serves as a guide to the eye.

TABLE II. Superconducting and normal ($n$) state quantities for $Y_{4.5}M_{0.5}Rh_6Sn_{18}$: Electronic specific heat coefficient $\gamma_0^{(n)}$ (cgs) obtained from a linear dependence $C(T)/T = \gamma_0^{(n)} + \beta T^2$ vs $T^2$ at $T = 0$ ($T > T_c^\star$), where $\beta = N(12/5)\pi^4 R\theta_D^{-3}$, and $N$ is the number of atoms in formula units; Debye temperature $\theta_D$ and residual resistivity $\rho_n(0)$ approximated to $T = 0$; $n^{2/3}\frac{S}{S_F}$ calculated from Eq. (1); mean free path $l(0) = 1.27 \times 10^4[\rho_n(n^{2/3}S/S_F)]^{-1}$; GLAG coherence length $\xi_{GL}^{fv}$ (full value, fv), also calculated in the dirty ($d$) limit [49]; BCS coherence length $\xi^{BCS}(0) = 7.95 \times 10^{-17}(n^{2/3}\frac{S}{S_F})(\gamma_0 T_c)^{-1}$; GLAG penetration lengths $\lambda_{GL}^{fv}(0)$ [49]; Ginzburg-Landau parameter $\kappa_{GL}^{fv}(0)$; critical temperature $T_c$ and $T_c^\star$ (in parentheses are the initial temperatures of percolation path formation); the value of $\frac{dH_{c2}}{dT}$ at $T_c$ and $T_c^\star$. The last two columns show the electron-phonon coupling parameters $\lambda$ and $\lambda^\star$ for $T_c$ and $T_c^\star$ phases, respectively. The quantities marked with $\star$ are assigned to the inhomogeneous phase $T_c^\star$.

| $Y_{4.5}M_{0.5}Rh_6Sn_{18}$ | $\gamma_0^{(n)}$ | $\theta_D$ | $\rho_n(0)$ | $n^{2/3}\frac{S}{S_F}$ | $l(0)$ | $\xi_{GL}^{fv}(0)$ | $\xi^{BCS}(0)$ | $\lambda_{GL}^{fv}(0)$ | $\kappa_{GL}^{fv}(0)$ | $T_c$ | $T_c^\star$ | $dH_{c2}/dT$ | $dH_{c2}^\star/dT$ | $\lambda$ | $\lambda^\star$ |
|---|---|---|---|---|---|---|---|---|---|---|---|---|---|---|---|
| $M$ | [mJ/mol K$^2$] (ergs/cm$^3$ K$^2$) | (K) | ($10^{-6} \times \Omega$ cm) | ($10^{13} \times$ cm$^{-2}$) | (nm) | (nm) | (nm) | (nm) | | (K) | (K) | ($10^4 \times$ G/K) | ($10^4 \times$ G/K) | (±0.004) | (±0.004) |
| Ca | 22.2 (565) | 150 | 306 | 3.0 (4.1*) | 14 (10*) | 6 (6*) | 14 (14*) | 1014 | 138 | 3.09 | 4.0* (...) | −1.96 | −1.61* | 0.50 | 0.54 |
| Ti | 26.8 (692) | 152 | 160 | 3.1 (3.8*) | 24 (20*) | 8 (8*) | 13 (14*) | 960 | 119 | 2.71 | 3.18* (3.56) | −1.93 | −1.60* | 0.47 | 0.50 |
| Sr | 22.2 (506) | 145 | 406 | 2.9 (4.2*) | 11 (7*) | 7 (8*) | 15 (15*) | 1080 | 146 | 3.02 | 3.63* (5.63) | −1.98 | −1.57* | 0.50 | 0.53 |
| Y | 13.0 (331) | 160 | 343 | 1.6 (1.7*) | 23 (22*) | 8 (8*) | 12 (13*) | 1293 | 170 | 3.08 | 3.19* (3.82) | −1.89 | −1.69* | 0.48 | 0.49 |
| Zr | 13.4 (345) | 152 | 322 | 1.7 (1.8*) | 23 (22*) | 8 (8*) | 13 (13*) | 1238 | 167 | 3.19 | 3.26* (3.70) | −1.80 | −1.68* | 0.50 | 0.51 |
| La | 19.9 (513) | 176 | 20 | 2.1 (2.3*) | 302 (276*) | 8 (8*) | 11 (11*) | 1025 | 138 | 3.18 | 3.33* (3.67) | −1.76 | −1.61* | 0.48 | 0.50 |
| Lu | 16.1 (411) | 153 | 338 | 2.2 (2.4*) | 17 (16*) | 8 (8*) | 13 (14*) | 1115 | 150 | 3.27 | 3.32* (3.68) | −1.75 | −1.66* | 0.50 | 0.51 |

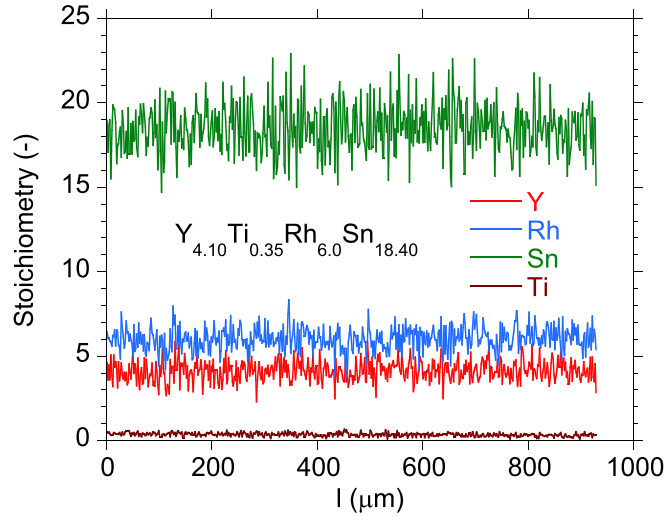


FIG. 3. Variation in stoichiometry of $Y_{4.1}Ti_{0.5}Rh_6Sn_{18.5}$ over the length of the sample. A very similar behavior was observed for all $Y_{4.1}M_{0.5}Rh_6Sn_{18.5}$ samples investigated here.

density $d \sim 8.1$ g/cm$^3$ is fully reached for these samples at temperatures $T < T_c$. The respective temperatures $T_c$, $T_c^\star$ and the temperature of the formation of separate inhomogeneous superconducting regions are summarized in Table II for the series of $Y_{4.5}M_{0.5}Rh_6Sn_{18}$ superconductors.

Figure 6 shows the specific heat $C(T)/T$ of $Y_{4.5}Ti_{0.5}Rh_6Sn_{18}$ at various magnetic fields (a) and the specific heat isotherms $C_T(B)$ divided by $T$ as a function of magnetic field (b), with linear behavior under the fields lower than $H_{c2}$. The linear $C_T(B)$ characteristics are usually

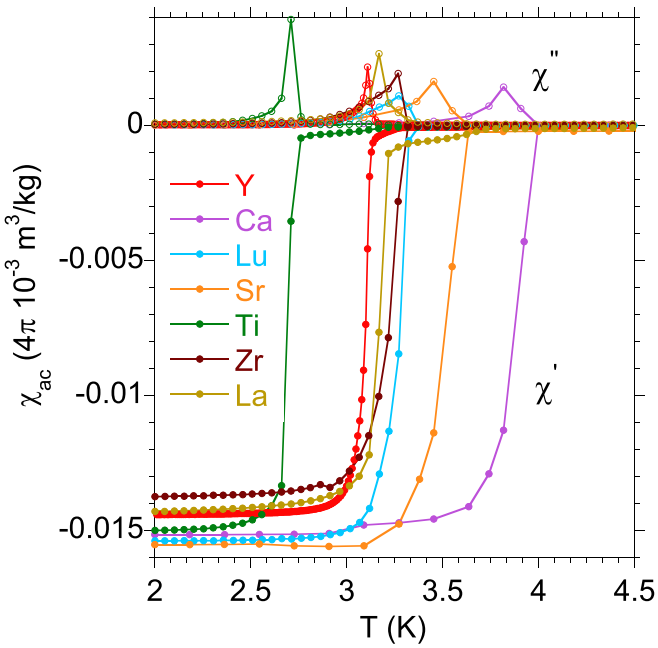


FIG. 4. Temperature dependencies of the real $\chi'$ and imaginary $\chi''$ components of the ac mass magnetic susceptibility $\chi_{ac}$ per 1 Oe for the series of $Y_{4.5}M_{0.5}Rh_6Sn_{18}$ compounds at $\nu = 100$ Hz. The used unit $4\pi \times 10^{-3}$ m$^3$/kg (SI) is equivalent to 1 emu/g (cgs).

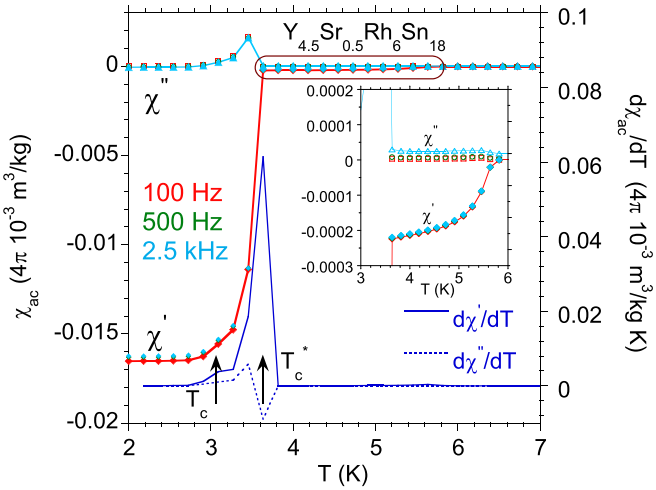


FIG. 5. Temperature dependencies of the real $\chi'$ and imaginary $\chi''$ components of the ac mass magnetic susceptibility $\chi_{ac}$ per 1 Oe for $Y_{4.5}Sr_{0.5}Rh_6Sn_{18}$, measured at different frequencies $\nu$, and derivative $d\chi'/dT$ and $d\chi''/dT$. The main maximum in $d\chi'/dT$ marked by an arrow is assigned to $T_c^\star = 3.63$ K of the inhomogeneous phase; the second weak maximum at 3.02 K marked by an arrow is referred to the formation of the bulk $T_c$ phase. The inset shows a broad transition at 5.63 K to the state with separate superconducting regions which, however, do not form a continuous path across the system (the same $\chi_{ac}$ units as in the main panel). Similar $\chi_{ac}(T)$ behavior was observed for remaining compounds; cf. Table II.

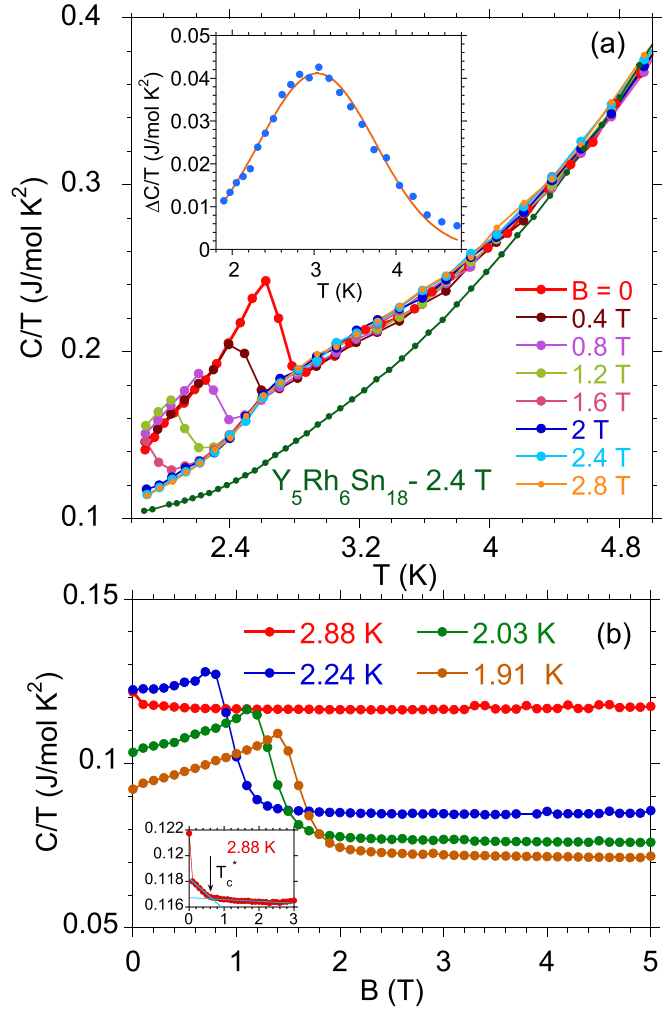


FIG. 6. (a) Temperature dependence of specific heat, $C(T)/T$, for $Y_{4.5}Ti_{0.5}Rh_6Sn_{18}$ at various magnetic fields. The data are compared with the $C(T)/T$ measured for $Y_5Rh_6Sn_{18}$ at the field of 2.4 T. The inset displays $\Delta C(T)/T$ well approximated by function $f(\Delta)$ with the following parameters: $\Delta_0 = 3.04$ K and variance $D = 0.5$ K$^2$, where $\Delta C(T) = C_{Ti}(T, B = 2.4\text{ T}) - C_{Y_5Rh_6Sn_{18}}(T, B = 2.4\text{ T})$. (b) The $C$ isotherms as a function of magnetic field $B$ for $Y_{4.5}Ti_{0.5}Rh_6Sn_{18}$. The inset shows the details in $C/T$ vs $B$ at $T_c$ in an extended scale; the units are the same.

attributed to the $s$-wave one-band superconductivity. Similar $C_B(T)$ and $C_T(B)$ dependencies were documented too for the remaining $Y_{4.5}M_{0.5}Rh_6Sn_{18}$ compounds; moreover, the $C$ data give evidence of nanoscale inhomogeneity, which is a reason for the appearance of the *high-temperature inhomogeneous superconducting phase* with characteristic critical temperature $T_c^\star > T_c$, as shown for sample $M =$ Sr in Fig. 7 (cf. Table II). Usually, the superconducting transition at $T_c^\star$ is accompanied by a weak feature in the $C(T)/T$ data (see Fig. 7). Despite this, specific heat and various experimental techniques (resistivity, susceptibility) always clearly separate the bulk and the inhomogeneous superconducting phase, as shown as an example for $Y_{4.5}Ca_{0.5}Rh_6Sn_{18}$ in Fig. 8.

In locally disturbed systems due to atomic disorder a metal-superconductor transition at $T_c^\star$ is broad and weakly visible in the $C(T)$ plot (cf. [45,46]). To determine the contribution of local inhomogeneous doping effect $\Delta C(T)$ resulting from the substitution of Y by metal $M$, first we assumed the same nanoscale inhomogeneity for $Y_5Rh_6Sn_{18}$ and for each $Y_{4.5}M_{0.5}Rh_6Sn_{18}$ sample due to atomic disorder over length scales similar to coherence $\xi$; next the specific heat $C(T)$ data at the magnetic field of 2.4 T were subtracted by $C(T)$ measured at the same field for the reference $Y_5Rh_6Sn_{18}$ sample. It is worth noting that the anomaly at $T_c^\star$ marks the onset of an inhomogeneous superconducting phase with spatial distribution of the magnitude of the superconducting energy gaps, though isolated superconducting islands can be formed at slightly higher temperatures. One can note, however, that $C(T)$ of $Y_{4.5}Ti_{0.5}Rh_6Sn_{18}$ behaves differently; namely, the broad maximum in its $C(T)/T$ data is much more pronounced in comparison to those of the remaining compounds of the series, with the maximum value of $\Delta C/T \approx 42$ mJ/mol K$^2$ at $T_c^\star$, as shown in Fig. 6(a). Following Ref. [44], a simple Gaussian gap distribution $f(\Delta) \propto \exp[-\frac{(\Delta-\Delta_0)^2}{2D}]$ approximates the specific heat $\Delta C/T$ data at around $T_c^\star$, where $\Delta_0$ and variance $D$ of the distribution are treated as fitting parameters. For $T < T_c$, $C/T$ experimental data are well fitted by the expression $C(T)/T = \gamma_0 + \beta T^2 + A/T \exp[-\Delta(0)/k_BT]$ with the electronic specific heat coefficient $\gamma_0 = 26$ mJ/mol K$^2$, lattice contribution with $\beta = 18$ mJ/mol K$^4$, and energy gap $\Delta(0) = 3.4$ K at $T = 0$, after subtracting the effect of disorder. Usually, the strong lattice disorder like this, observed for Ti dopant, destroys the long-range order of the flux-line lattice, after which only short-range order prevails. If the applied magnetic field increases for a fixed temperature, then a

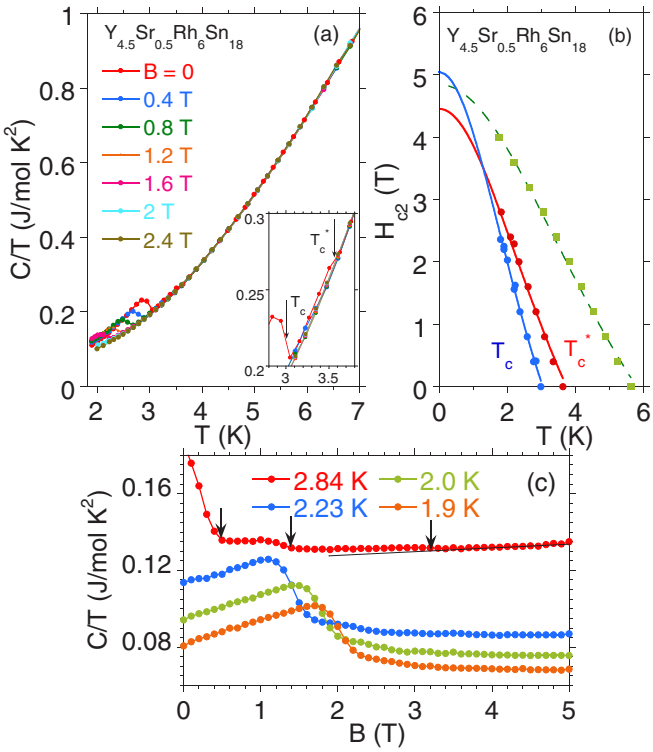


FIG. 7. (a) Temperature dependence of specific heat, $C(T)/T$, for $Y_{4.5}Sr_{0.5}Rh_6Sn_{18}$ at various magnetic fields. The inset shows the details in $C/T$ vs $T$ near $T_c^\star$ in an extended scale; the units are the same as in panel (a). Panel (b) exhibits temperature dependencies of the upper critical field for the bulk ($T_c$) and disorder ($T_c^\star$) phases. The green points in the $H$-$T$ plot indicate formation of disconnected superconducting regions, which give the superconducting transition a percolation path upon forming. The $H$-$T$ data are approximated by the Ginzburg-Landau (GL) model: $H_{c2}(T) = H_{c2}(0)\frac{1-t^2}{1+t^2}$, and $t = T/T_c$ (lines). Panel (c) shows heat capacity $C$ isotherms as a function of magnetic field. The arrows indicate the respective critical fields for the phases described in panel (b).

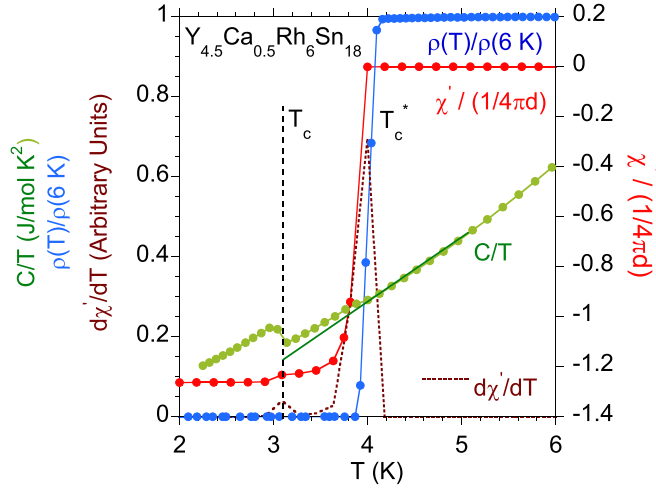


FIG. 8. For the purpose of comparison, the ac susceptibility, electrical resistivity, and specific heat are displayed for $Y_{4.5}Ca_{0.5}Rh_6Sn_{18}$. The data from various experiments clearly show the superconducting bulk phase below $T_c$ and the inhomogeneous $T_c^\star$ phase. Similar results were obtained for other dopants $M$.

phase transition between the short-range order and disorder in the vortex system eventually could occur due to the enormous increase of the lattice defects inside the short-range domains, which could induce the peak effect.

Figure 7(b) shows the temperature dependence of the upper critical field for the $T_c$ and $T_c^\star$ phases of $Y_{4.5}Sr_{0.5}Rh_6Sn_{18}$, also shown the $H_{c2}(T)$ behavior for the inhomogeneous phase with the formation of the superconducting regions, however, without continuous percolation path across the system. The respective $H$-$T$ data are well approximated by the Ginzburg-Landau equation $H_{c2}(T) = H_{c2}(0)\frac{1-t^2}{1+t^2}$ giving for the respective $T_c^\star$ and $T_c$ phases $H_{c2}^\star < H_{c2}$ and different $\frac{dH_{c2}}{dT}$ near the critical temperature $T_c$ or $T_c^\star$. Previously [19] we have documented that in the presence of lattice disorder and the effect of breaking the lattice periodicity due to doping, similar $H$-$T$ behaviors can be described by the percolation model. We assumed that the inhomogeneous system, where the local critical temperature $T_c^{(i)}$ is continuously spread over some range, can be analyzed as a random resistor network (RRN) [47,48] and the dependence between $H_{c2}^{(i)}$ and $T_c^{(i)}$ is linear. $H_{c2}^{(i)} = aT_c^{(i)} + b$ with parameters $a < 0$ and $b$ have been determined by fitting to the experimental data. $T_c^{(i)}$ is defined as the temperature at which the superconducting regions characterized by the upper critical field $H_{c2}^{(i)}$ form a percolation path across the sample. This simple approach turns out to give a perfect agreement of model predictions with experimental data for $La_3Rh_4Sn_{13}$ [19]. The RRN model is also adequate to describe the $H$-$T$ behavior of the $Y_{4.5}M_{0.5}Rh_6Sn_{18}$ series with $M$ = Ca, Sr, and Ti.

The above experimental data allowed us to obtain the parameters characteristic of the superconducting and normal state for the $Y_{4.5}M_{0.5}Rh_6Sn_{18}$ compounds with predictions of the Ginzburg-Landau-Abrikosov-Gorkov (GLAG) theory of the type-II superconductivity ($\kappa > 1/\sqrt{2}$); some of them important for characterizing the superconductivity of the samples are listed in Table II. The samples are found as moderate dirty alloys with $\xi \approx l$. According to Ref. [49], all parameters are calculated as a *full value* (or for a dirty limit $\xi \gg l$), and are listed in Table II. In the frame of GLAG theory [50] the slope of $\frac{dH_{c2}}{dT}$ at $T_c$ in the units G/K is

$$-\left.\frac{dH_{c2}}{dT}\right|_{T=T_c} = \left[9.55\times10^{24}\gamma_0^2 T_c\left(n^{2/3}\frac{S}{S_F}\right)^{-2} + 5.26\times10^4\gamma_0\rho_n\right][R(\lambda_{tr})]^{-1}, \quad (1)$$

where $n$ is the density of conduction electrons in $cm^{-3}$, $S/S_F$ is the ratio of the real Fermi surface $S$ to the surface $S_F = 4\pi(3\pi^2 n)^{3/2}$ of the free electron gas, and the Gorkov function $R(\lambda_{tr}) \approx 1$ for $\lambda_{tr} \to 0$ [$\lambda_{tr} \sim \xi(0)/l(0) = 5.51\times10^{-21}\rho_n(n^{2/3}S/S_F)(\gamma_0 T_c)^{-1} \approx 0$ for all samples]. Then, the estimate of $n^{2/3}(S/S_F)$ allowed us to calculate the Ginzburg-Landau coherence length $\xi_{GL}^{fv}$, the GL penetration depth $\lambda_{GL}^{fv}$,

and the GL parameter $\kappa_{\rm GL}^{\rm fv}(0)$ [49]:

$$\xi_{\rm GL}^{\rm fv} = \left[2.90\times10^{32}(T_c\gamma_0)^2\left(n^{2/3}\frac{S}{S_F}\right)^{-2} + 1.60\times10^{12}\rho_n\gamma_0 T_c\right]^{-1/2}[R(\lambda_{\rm tr})]^{1/2}(1-t)^{-1/2}, \quad (2)$$

$$\lambda_{\rm GL}^{\rm fv} = \left[8.77\times10^{15}\gamma_0\left(n^{2/3}\frac{S}{S_F}\right)^{-2} + 4.83\times10^{-5}\rho_n T_c^{-1}\right]^{1/2}[R(\lambda_{\rm tr})]^{-1/2}(1-t)^{-1/2}, \quad (3)$$

$$\kappa_{\rm GL}^{\rm fv} \equiv \lambda_{\rm GL}(0)/\xi_{\rm GL}(0) = \left[1.60\times10^{24}T_c\gamma_0^{3/2}\left(n^{2/3}\frac{S}{S_F}\right)^{-2} + 8.78\times10^{3}\gamma_0^{1/2}\rho_n\right][R(\lambda_{\rm tr})]^{-1} \gg 1. \quad (4)$$

It is worth noting that $\xi_{\rm GL}^{d}(0) \sim \sqrt{\xi_0^{\rm BCS} l(0)}$ is between 13 nm ($M$ = Sr) and 18 nm ($M$ = Ti) [for La, $\sqrt{\xi_0^{\rm BCS} l(0)} = 58$ nm] and predicts the moderate disorder regime ($\xi \gtrapprox l$) for the investigated samples. Within the BCS theory

$$T_c = 1.14\langle\omega\rangle \exp\{-1/[N(\epsilon_{\rm F})U]\}, \quad (5)$$

where $N(\epsilon_F)$ is the density of states (DOS) at the Fermi energy in states/(eV spin), $\langle\omega\rangle \sim \theta_D/1.2$, and $N(\epsilon_F)U$ is approximately [51]

$$N(\epsilon_F)U \to \frac{\lambda-\mu^\star}{1+\lambda}. \quad (6)$$

In Eq. (6) $\mu^\star$ is the Coulomb pseudopotential of Morel and Anderson [52],

$$\mu^* = \frac{N(\epsilon_F)U}{1+N(\epsilon_F)U\ln(E_B/\omega_0)}, \quad (7)$$

and the electron-phonon coupling parameter [53,54]

$$\lambda = \frac{N(\epsilon_F)\langle I^2\rangle}{M_A\langle\omega^2\rangle}, \quad (8)$$

where $\langle I^2\rangle$ is the square of the electronic matrix element of electron-phonon interactions averaged over the Fermi surface, $M_A$ is the atomic mass, $E_B$ is the electronic bandwidth, and $\omega_0$ is the maximum phonon frequency. To calculate the $\lambda$'s and $\lambda^\star$'s listed in Table II, we used the expression

$$N(\epsilon_F)U = \frac{-[2+\lambda(1-x)] + [\lambda^2(1+x)^2+4\lambda+4]^{1/2}}{2x(1+\lambda)}, \quad (9)$$

by combining Eqs. (6) and (7), where $x = \ln(E_B/\omega_0)$, and $E_B \sim 4.5$ eV is the calculated conduction band width. Expression (5) allows us to obtain an *experimental* value of $N(\epsilon_F)U$ and $[N(\epsilon_F)U]^\star$ for the respective $T_c$ and $T_c^\star$ phase, while Eq. (9) gives the $\lambda$-dependent variable $N(\epsilon_F)U$. A self-consistent procedure allowed us to calculate the $\lambda$'s listed in Table II for the best agreement between calculated and experimentally obtained $N(\epsilon_F)U$. Within the series of the $Y_{4.5}M_{0.5}Rh_6Sn_{18}$ superconductors, the electron-phonon coupling $\lambda^\star$ parameters obtained for Ca, Ti, and Sr dopants are evidently larger than the respective $\lambda$'s, determined for their bulk superconducting phases below $T_c$. This is a characteristic behavior of a number of isostructural disordered quasiskutterudites (cf. Ref. [19]), where the difference between the electron-phonon coupling parameters for the two superconducting phases $\Delta\lambda = \lambda^\star - \lambda > 0$ reflects the emergence of the higher-$T_c$ state, as well as characterizes the degree of local chemical disorder. One also notes that the largest values of $\Delta\lambda$ well correlate with the percolative superconductivity of Ca, Ti, and Sr dopants, while this is not the case for Zr, La, or Lu having $\Delta\lambda \sim 1\times10^{-2}$ very small (see Table II).

### C. Comparison of the resistivity data; observation of the peak effect

In the course of our detailed research of skutterudite-related 3 : 4 : 13- and 5 : 6 : 18-type superconductors, we have documented how much nonmagnetic disorder in these materials can raise $T_c$. Below, we analyze how much the local inhomogeneous doping effect and the associated lattice stress can affect the nature of superconductivity and the value of $T_c$ in these quasiskutterudites. For this purpose, the yttrium in $Y_5Rh_6Sn_{18}$ is partially replaced with various metals $M$ from the same as Y or neighboring groups in the periodic table, which allowed us to determine the impact of metal $M$ valence states and/or its atomic radii on the resistivity of $Y_{4.5}M_{0.5}Rh_6Sn_{18}$.

Figure 9 shows the resistivity $\rho(T)$ for the series of $Y_{4.5}M_{0.5}Rh_6Sn_{18}$ compounds. The resistivity drop indicates the superconducting transition at $T_c^\star$ ($T_c^\star \gtrapprox T_c$; cf. Table II). The $\rho(T)$ characteristics indicate some interesting effects in both the superconducting and the *normal metallic* state:

(i) The $\rho(T)$ behavior in the normal metallic state is for $Y_{4.5}Ti_{0.5}Rh_6Sn_{18}$ and $Y_{4.5}La_{0.5}Rh_6Sn_{18}$ typical for metals [55,56], while the resistivity of the remaining superconductors with dopants $M$ = Y, Ca, Sr, Zr, and Lu indicates their semimetallic nature and exhibits a negative temperature coefficient of resistance (TCR) $d\rho/dT < 0$ in a wide temperature range 70 K $\lesssim T \lesssim$ 300 K with $\ln\rho \sim T^{-1/4}$ dependence (as shown in the inset to Fig. 9). This unusual $\rho \propto \exp[(\frac{\Delta_M}{k_B T})^{1/4}]$ behavior is known as the Mott variable-range hopping effect [57,58], where $\Delta_M$ is a pseudogap in the band structure near the Fermi level. Indeed, our previous *ab initio* calculations for several similar quasiskutterudites ($La_3Co_4Sn_{13}$ [59], $Ce_3Co_4Sn_{13}$ [60], $Lu_5Rh_6Sn_{18}$ [42]) documented the pseudogap with very small DOS, located in the bands of these compounds at a similar binding energy of $\sim -0.3$ eV. Even a small number of vacancies shifts this pseudogap toward the Fermi level; simultaneously, the presence of defects may reduce the pseudogap after its shift to $\epsilon_F$ (this is characteristic of Kondo insulators; see, e.g., [61]). We expect a similar band-structure effect for the off-stoichiometry $Y_{4.5}M_{0.5}Rh_6Sn_{18}$ samples, which in consequence of vacancies show semimetallic $\rho(T)$ behavior with accompanying Mott variable-range hopping effect in the metallic state.

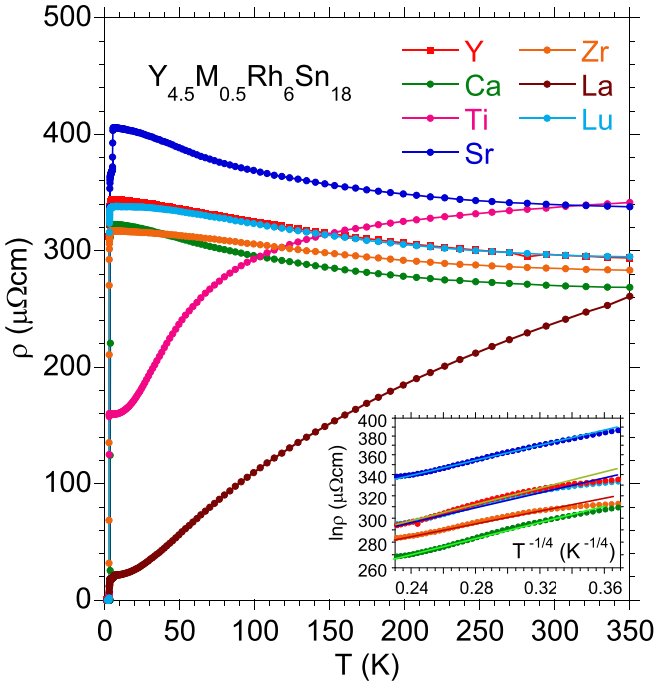


FIG. 9. Electrical resistivity $\rho$ as a function of temperature at $B = 0$ for the series of $Y_{4.5}M_{0.5}Rh_6Sn_{18}$ superconductors, where $M$ = Y, Ca, Ti, Sr, Zr, La, and Lu. The inset displays the resistivity data in coordinates $ln\rho = f(T^{-1/4})$. The lines approximate the linear $ln\rho$ vs $T^{-1/4}$ behavior in the temperature range between ~80 K and ~300–350 K, depending on the sample.

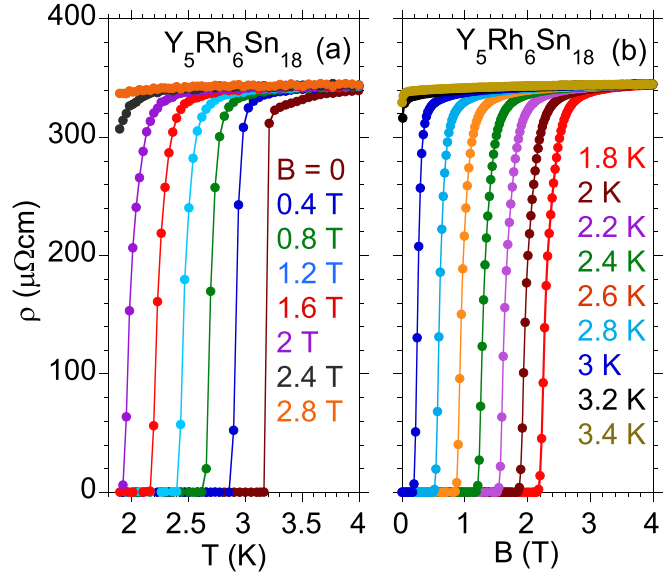


FIG. 10. Low-temperature electrical resistivity, $\rho$, for $Y_5Rh_6Sn_{18}$ for a measuring current of 10 mA. Panel (a) shows $\rho_B(T)$; panel (b) exhibits isotherms of $\rho$ as a function of the magnetic field. Analogous behaviors in $\rho_B(T)$ and $\rho_T(B)$ have been demonstrated in the temperature region $T < T_c^\star$ for $Y_{4.5}M_{0.5}Rh_6Sn_{18}$ with $M$ = Ca and Lu. Here, $T_c^\star$ is defined as the temperature corresponding to midpoint of the resistive transition at zero magnetic field.

(ii) Figures 10 and 11 depict temperature-dependent resistivity at various magnetic fields, as well as magnetoresistance isotherms in the superconducting state for Y and Ti samples, respectively. The $\rho_B(T)$ and $\rho_T(B)$ characteristics shown in Fig. 10 are quite different from those in Fig. 11, which suggests a strong relationship between the superconducting nature of the $Y_{4.5}M_{0.5}Rh_6Sn_{18}$ sample and the atomic radius of metal $M$.

For $M$ = Y, Ca, and Lu [Fig. 10(a)] $\rho$ exhibits a sharp drop below $T_c^\star$ with the transition width less than 0.1 K, which attests to good sample quality. A considerable broadening and suppression of the superconducting transition with increasing magnetic fields are observed until the superconducting state completely disappears. Likewise, magnetoresistance isotherms for $Y_{4.5}M_{0.5}Rh_6Sn_{18}$, where $M$ = Y, Ca, or Lu, are typical of BCS superconductors, as shown in Fig. 10(b). Here, one can note that the atomic radius of metal $M$ is comparable to (Lu case) or larger than (Ca) the yttrium one.

The $\rho_B(T)$ and $\rho_T(B)$ characteristics for $Y_{4.5}Ti_{0.5}Rh_6Sn_{18}$ are shown in Fig. 11. Panel (a) shows the temperature-dependent $\rho$ under various magnetic fields. The sample goes to the *disorder-enhanced* superconducting phase at $T_c^\star$ = 3.18 K ($B = 0$) and then to the *bulk superconducting state* at $T_c = 2.71$ K. In the fields larger than ~0.4 T the superconducting transition broadens and it is difficult to separate the $T_c^\star$ phase from the $T_c$ one. In the magnetic fields regime $B > 1.2$ T the $\rho_B(T)$ curves under different fields intersect with each other, which indicates an anomalous behavior of the magnetoresistance in this sample. Figure 11(b) shows the magnetoresistance isotherms vs increasing magnetic field. As the applied field increases, the $\rho$ isotherm of $Y_{4.5}Ti_{0.5}Rh_6Sn_{18}$ measured at $T = 1.8$ K suddenly rises, reaching a peak before finally dropping to a minimal value (almost zero). A similar tendency in the field dependence of $\rho_B(T)$ can also be visible in the higher temperatures up to $T = 2.8$ K. This field-induced reentered superconductivity is expected to be suppressed at $B > 2.4$ T [see Figs. 11(b) and 12]. A similar field-induced peak effect in the superconducting state is also observed for $Y_{4.5}Zr_{0.5}Rh_6Sn_{18}$ between 2.2 K and 3 K as shown in Fig. 13(b); however, this PE behavior is not as pronounced as for the sample with Ti dopant.

The PE anomalies in the resistance of $Y_{4.5}Ti_{0.5}Rh_6Sn_{18}$ are more clearly seen in the variation of normalized resistance $R/R_n$ as a function of magnetic field at $T = 1.9$ K, where $R_n$ is the normal state resistance obtained slightly above $T_c^\star$. The magnetic fields at which these anomalies appear are strongly dependent on the measuring current, as shown in Fig. 14. This field-dependent behavior of resistance under various measuring currents is a key phenomenon for interpreting the resistance anomaly as a peak effect.

Figure 15 shows the isothermal magnetic-field change of the real ($\chi'$) and imaginary ($\chi''$) components of the ac susceptibility for $Y_{4.5}Ti_{0.5}Rh_6Sn_{18}$. As the field increases, $\chi'$ isotherms measured for $T = 1.8$ K or at 2 K show a weak maximum at $B = 1.4$ T or 1.1 T, respectively. Similarly, $\chi''$ shows the maxima related to the respective extremes of $\chi'$. The peaks in $\chi_{ac}$ were found to be independent of frequency; also the curves shown in Fig. 15 were reversible for increasing and decreasing fields. Such a $\chi_{ac}$ behavior is characteristic of the peak effect in superconductors.

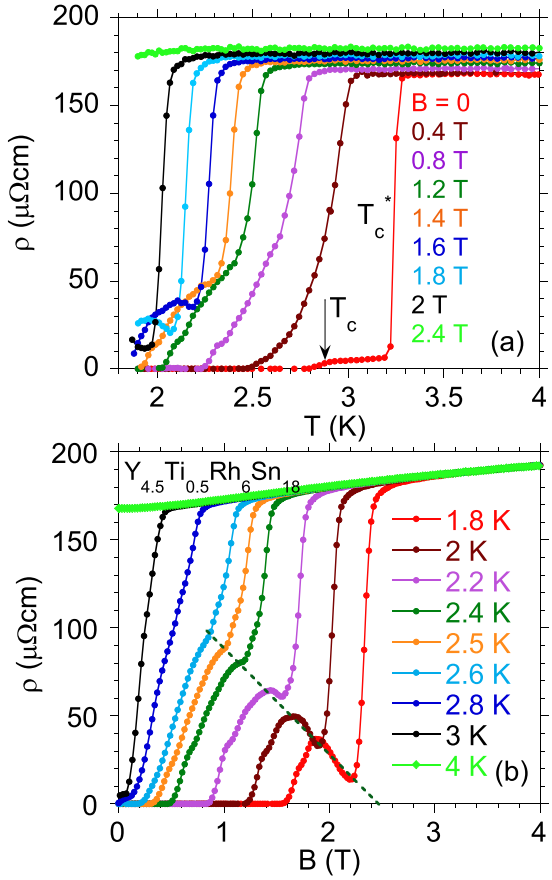


FIG. 11. (a) Electrical resistivity for $Y_{4.5}Ti_{0.5}Rh_6Sn_{18}$ for a measuring current of 10 mA. Panel (a) shows the low-temperature dependence of $\rho$ when the magnetic field is in the range of $0 \leqslant B \leqslant 2.4$ T. The resistivity drop at $B = 0$ indicates the superconducting transition at $T_c^\star$, while the weak change of $\rho$ at ∼2.8 K is related to the bulk transition at $T_c$. For the fields $B > 0.4$ T the resistivity shows an anomalous rise in the SC state. (b) Magnetoresistance isotherms of $Y_{4.5}Ti_{0.5}Rh_6Sn_{18}$ as a function of applied magnetic field for the temperature changing from 1.8 to 4 K with the appearance of the anomalous peak effect in $\rho$. At $T = 1.8$ K $\rho$ first increases with rise of the magnetic field, then a reentrance of superconductivity happens at $B \approx 2.2$ T. As the temperature increases, the "reentrance" behavior becomes less and less obvious and finally disappears at $T > 2.6$ K. At the lowest temperatures the effect is expected to be observed for the magnetic field $B < 2.4$ T. The dashed line shows the estimated critical field, below which the peak effect coexists with the SC state.

The resistivity of $Y_{4.5}Sr_{0.5}Rh_6Sn_{18}$ shows at $T_c^\star$ a narrow transition between the normal and superconducting state, as shown in Fig. 16(a), while between $T_c^\star$ and 5.6 K the figure exhibits an abnormal change in $\rho(T)$, which indicates formation of disconnected superconducting regions in the sample and suggests the percolation modeling for this inhomogeneous superconductor. As long as the zero-resistivity elements do not form a continuous path across the system, the sample remains in the normal state, but with decreasing resistivity, as shown in Fig. 16. The magnetoresistance isotherms shown in panel (b) do not exhibit the peak effect, but indicate the superconductivity preceded by the creation of activating percolation paths between ∼6 K and $T_c^\star$. Recently [19], we

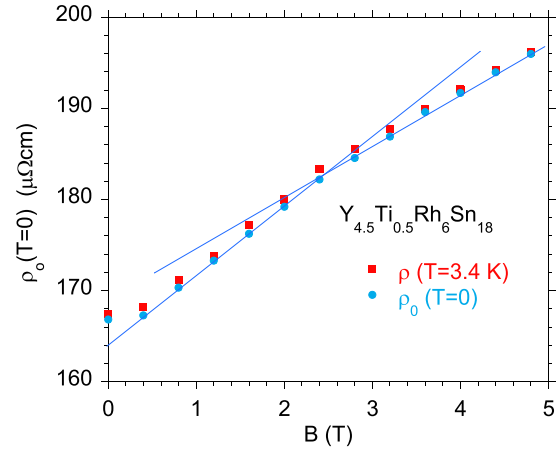


FIG. 12. $Y_{4.5}Ti_{0.5}Rh_6Sn_{18}$; electrical resistivity $\rho_0$ approximated from the normal state near $T_c^\star$ to $T = 0$ vs magnetic field. The field of 2.4 T separates different slopes in $\rho_0(B)$ behavior; cf. Fig. 11(b).

proposed a percolation approach based on the random resistor network (RRN) model [47,48], that can reproduce similar temperature dependence of $H_{c2}$ in analogous quasiskutterudites with $T_c^\star$ significantly larger than $T_c$ and $|\frac{dH_{c2}}{dT}| > |\frac{dH_{c2}^\star}{dT}|$ dependence near proper critical temperatures, where the single-band (or multiband) Werthamer-Helfand-Hohenberg

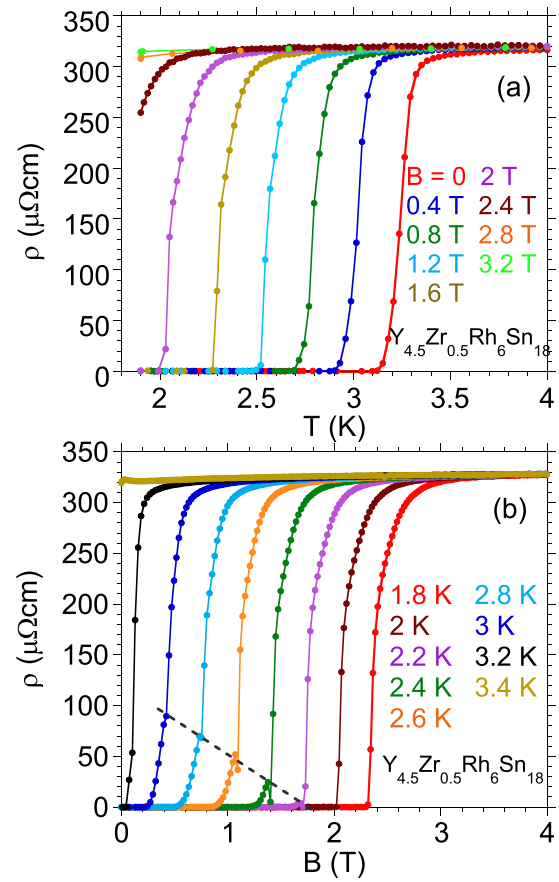


FIG. 13. Electrical resistivity $\rho$ for $Y_{4.5}Zr_{0.5}Rh_6Sn_{18}$ below $T_c^\star$ for a measuring current of 10 mA. Panel (a) shows $\rho_B(T)$; panel (b) displays isotherms of $\rho$ as a function of the magnetic field.

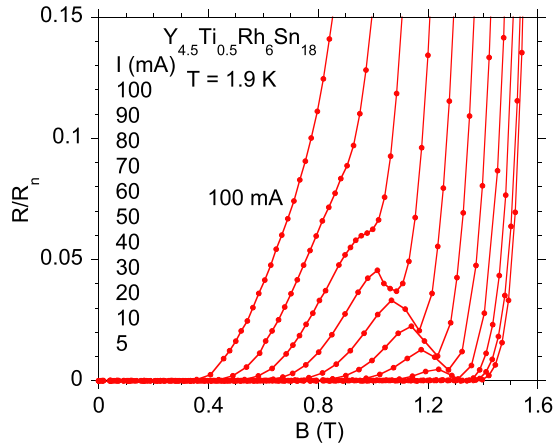


FIG. 14. Field-dependent normalized resistance $R/R_n$ of $Y_{4.5}Ti_{0.5}Rh_6Sn_{18}$ for different measuring currents at 1.9 K.

[50] theory cannot explain the *H-T* experimental data (cf. Sec. III B).

(iii) The comprehensive results obtained for the series of the $Y_{4.5}M_{0.5}Rh_6Sn_{18}$ superconductors allow us to construct a simple modeling of superconductivity with the presence of the PE phase, taking into account the local stresses caused by *M* dopant with the atomic radius smaller than the radius of Y. The peak effect in the superconducting state is only possible when the radius of metal *M* is smaller then the radius of Y. We have shown, too, that the electronic properties of the impurity *M* significantly affect the nature of electrical conductivity of sample; however, the change of the band structure near $\epsilon_F$ due to doping is not the cause of the reentrance in superconductivity phenomenon. This will be discussed in Sec. IV.

### D. The peak effect induced by vacancies in the isostructural $Lu_{5-\delta}Rh_6Sn_{18}$; band structure calculations

In the doped $Y_{4.5}M_{0.5}Rh_6Sn_{18}$, the magnetic field induced reentrance of superconductivity has been observed only for the dopants smaller than the yttrium atoms. One can conclude that the peak effect results from local stresses; if such

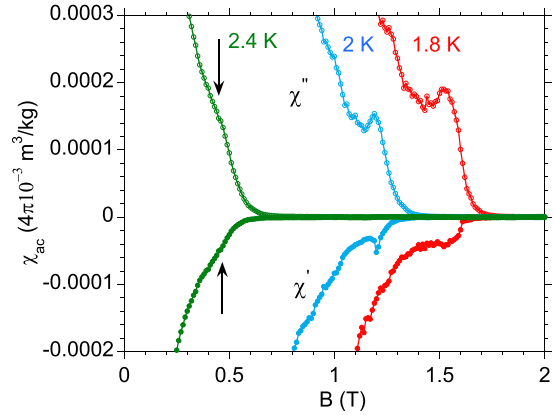


FIG. 15. $Y_{4.5}Ti_{0.5}Rh_6Sn_{18}$; real ($\chi'$) and imaginary ($\chi''$) parts of the ac susceptibility as a function of applied dc magnetic field. The curves are reversible for increasing as well as decreasing fields.

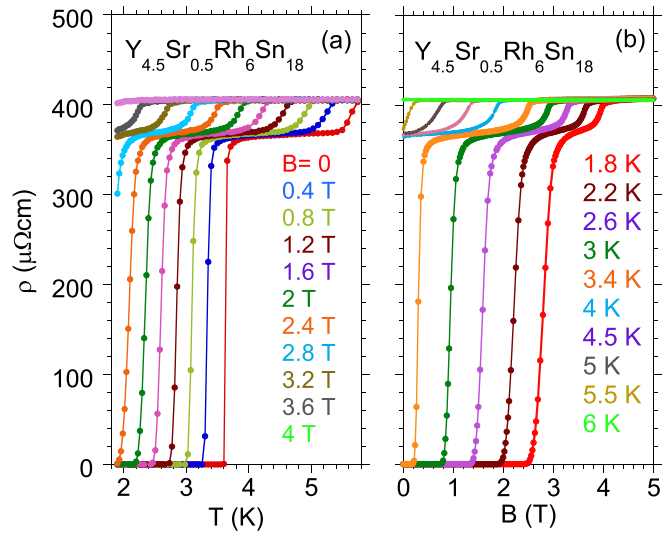


FIG. 16. Electrical resistivity $\rho$ for $Y_{4.5}Sr_{0.5}Rh_6Sn_{18}$ for a measuring current of 10 mA. Panel (a) shows $\rho_B(T)$; panel (b) displays isotherms of $\rho$ as a function of the magnetic field. The change of $\rho$ between $T_c^\star = 3.63$ and $T = 5.63$ K ($B = 0$) indicates formation of disconnected superconducting regions. Similar $\rho_B(T)$ characteristics are observed for $Y_{4.5}La_{0.5}Rh_6Sn_{18}$.

a hypothesis is correct, the effect should also be generated by the presence of vacancies in the 32(*g*) sites of the parent compound [35]. Continuing, first, the analysis should be performed for the reference system $Y_{4.5}Rh_6Sn_{18}$ with vacancies at Y sites; unfortunately we were unable to obtain a single-phase compound. However, it is possible to obtain isostructural superconductor $Lu_5Rh_6Sn_{18}$ and its off-stoichiometric equivalent [42]. Microanalysis has documented [42] that the system 5 : 6 : 18 does not crystallize in an assumed stoichiometry but forms a $Lu_{5-\delta}Rh_6Sn_{18}$ phase with Lu deficiency $\delta \ll 1$. Figure 17(a) shows the magnetoresistance for $Lu_{5-\delta}Rh_6Sn_{18}$. The anomalous rise in $\rho_T(B)$ is not explicitly observed in the superconducting state for the system with composition closed to assumed stoichiometry (5 : 6 : 18) [62], while the peak effect is clearly seen for sample $Lu_{4.6}Rh_6Sn_{18}$ with the number of vacancies much larger than $\delta$ [see Fig. 17(b)]. Analogously, quite different temperature characteristics of $\rho$ observed for $Lu_5Rh_6Sn_{18}$ (typical of metals) or $Lu_{4.5}Rh_6Sn_{18}$ (semimetallic) [42] are also documented for a series of Y-based superconducting quasiskutterudites, as shown in Fig. 9; they are typical for metals (the case of $M =$ Ti, La) or show the $\rho \sim T^{-1/4}$ behavior for $M =$ Y, Ca, Sr, Zr, or Lu. The comparable behavior in the respective $\rho(T)$ plots of the Lu- and Y-based systems suggests a significant impact of the density of states at the Fermi level on electric transport. We therefore compare the band structure calculations for $Lu_5Rh_6Sn_{18}$ and $Lu_{4.5}Rh_6Sn_{18}$ having vacancies at Lu sites to understand the analogous properties of the doped $Y_{4.5}M_{0.5}Rh_6Sn_{18}$ compounds, and assuming that the local stress effect caused by the lower size of *M* in respect to Y and/or the vacancies at Y sites are similar in nature and could be a cause of the reentrant phenomenon (Figs. 18 and 19).

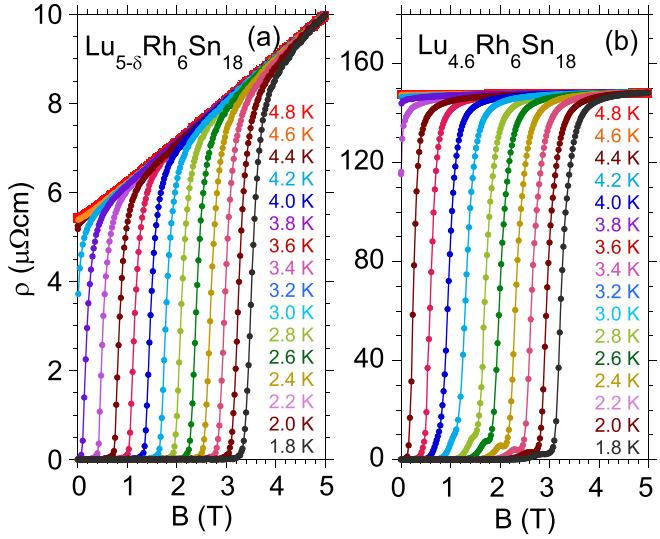


FIG. 17. Magnetoresistance isotherms for a measuring current of 10 mA as a function of applied magnetic field at different temperatures for $Lu_{5-\delta}Rh_6Sn_{18}$ with small Lu deficiency $\delta$ (a), and for off-stoichiometry $Lu_{4.6}Rh_6Sn_{18}$ (b). The peak in $\rho_T(B)$ in the superconducting state of $Lu_{4.6}Rh_6Sn_{18}$ occurs in the magnetic fields $B > 1$ T, while for the $Lu_{5-\delta}Rh_6Sn_{18}$ sample with the composition similar to 5 : 6 : 18 this behavior is not clearly observed.

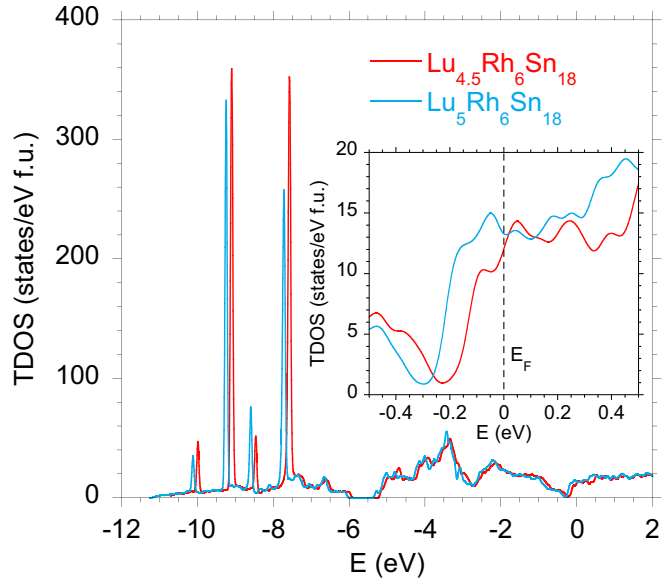


FIG. 19. The comparison of TDOS for $Lu_5Rh_6Sn_{18}$ and $Lu_{4.5}Rh_6Sn_{18}$. The inset shows details near the Fermi level. The DOSs were calculated for SO coupling and for $U_{4f} = 6.8$ eV and $U_d = 3$ eV giving the best comparison to the XPS valence band spectra (see Ref. [42]).

The *ab initio* calculations confirmed the significance of correlation energy $U$ on the energy of Lu $4f$ electronic states, while its impact on the shape of the total density of states (TDOS) between $-6$ eV and the Fermi energy was negligible. We chose for DFT calculations $U_f$ = (3, 4.5, 5.5, and 6.8) eV, respectively. For all calculations made for a number of different $U_f$, the $d$-electron correlations with $U_d = 3$ eV were always taken into account the same [63]. The Lu $4f$-electron XPS states are well accounted for by the Lu $4f$ states calculated for $U_f = 6.8$ eV (cf. Fig. 6 in Ref. [42]), which suggests that the DFT band structure calculations with $U_f = 6.8$ eV and accompanying $U_d = 3$ eV are the most reasonable for obtaining the details in the electronic bands near the Fermi level. For both samples the dispersive character of the calculated bands is similar; however, the partial DOSs of $Lu_{4.5}Rh_6Sn_{18}$ are shifted toward $\epsilon_F$ by ∼0.2 eV in respect to the bands calculated for stoichiometric $Lu_5Rh_6Sn_{18}$. The *ab initio* calculations thus also confirmed that the presence of vacancies shifts the pseudogap toward the Fermi level, thereby reducing the TDOS at $\epsilon_F$, as shown in Fig. 19. The formation of the pseudogap results from strong hybridization between the band states located on various surfaces of the Brillouin zone, as shown in Fig. 18 ($k$ lines: $Y$-Σ-Γ, $Z$-Σ1-$N$, $P$-$Y$1-$Z$).

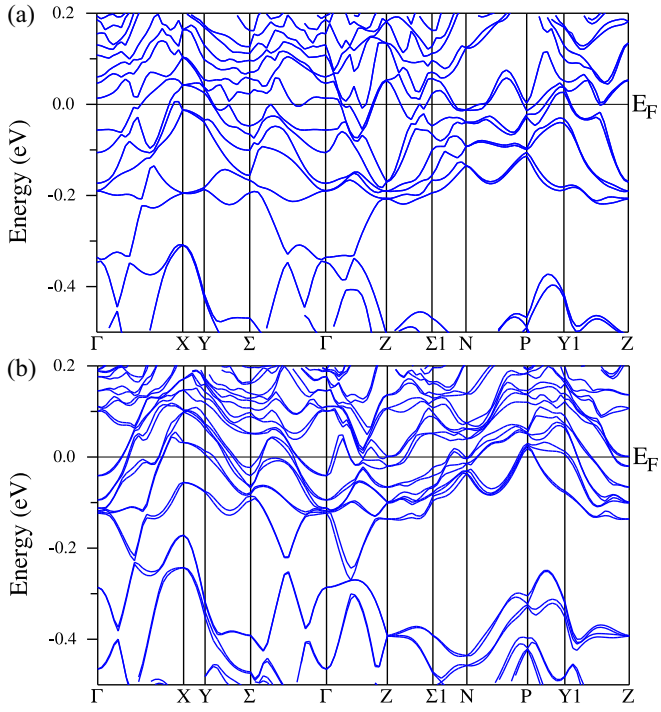


FIG. 18. The band structure calculated along high-symmetry $k$ lines in the Brillouin zone for stoichiometric $Lu_5Rh_6Sn_{18}$ (a) and $Lu_{4.5}Rh_6Sn_{18}$ (b). The bands are calculated for $U_{4f} = 6.8$ eV and $U_d = 3$ eV and spin-orbit (SO) coupling.

The pseudogap shift with increase of the number of defects toward the Fermi level justifies the observation of the negative TCR behavior in $\rho(T)$, as well as the Mott variable-range hopping effect for $Lu_{4.5}Rh_6Sn_{18}$ (cf. [42]) and for some $Y_{4.5}M_{0.5}Rh_6Sn_{18}$ samples (as shown in Fig. 9). However, the presence of the pseudogap at $\epsilon_F$ cannot be the main reason for the anomalous resistivity rise in the superconducting state of $Y_{4.5}M_{0.5}Rh_6Sn_{18}$, the more so as the PE phenomenon is also observed for *metallic* superconductors doped with La and Ti atoms. Therefore, the discussion of the PE reduced only to the band structure properties near $\epsilon_F$ seems not to be justified. The size effect of the impurity/vacancy seems to be crucial. For example, a strong peak effect has been observed for $Y_{4.5}Ti_{0.5}Rh_6Sn_{18}$, while its normal state resistivity

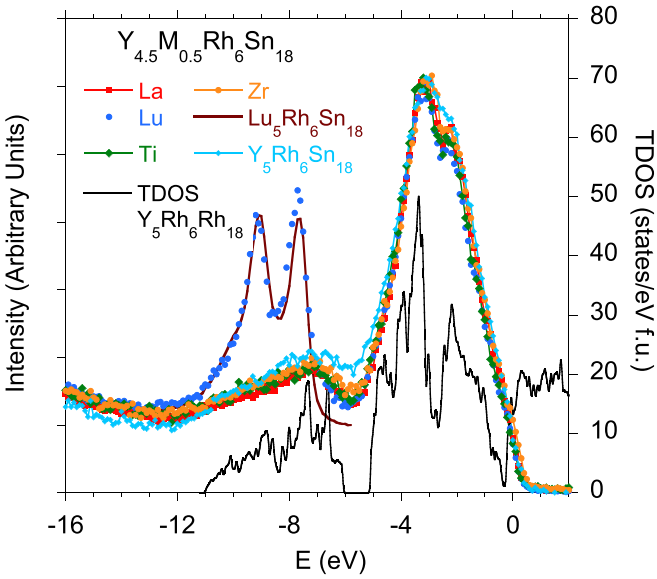


FIG. 20. Valence band XPS spectra for $Y_{4.5}M_{0.5}Rh_6Sn_{18}$ are compared with the calculated total DOS for pristine $Y_5Rh_6Sn_{18}$ (TDOS for $Y_5Rh_6Sn_{18}$ is taken from Ref. [41]). The intensities of all measured XPS bands are normalized to the background for $Y_5Rh_6Sn_{18}$ at $E > \epsilon_F$. Solid brown line represents the Lu $4f$ VB XPS spectra obtained for $Lu_5Rh_6Sn_{18}$ (see Ref. [42]), and normalized to VB XPS spectra of $Y_{4.5}Lu_{0.5}Rh_6Sn_{18}$ at $E = -12$ eV.

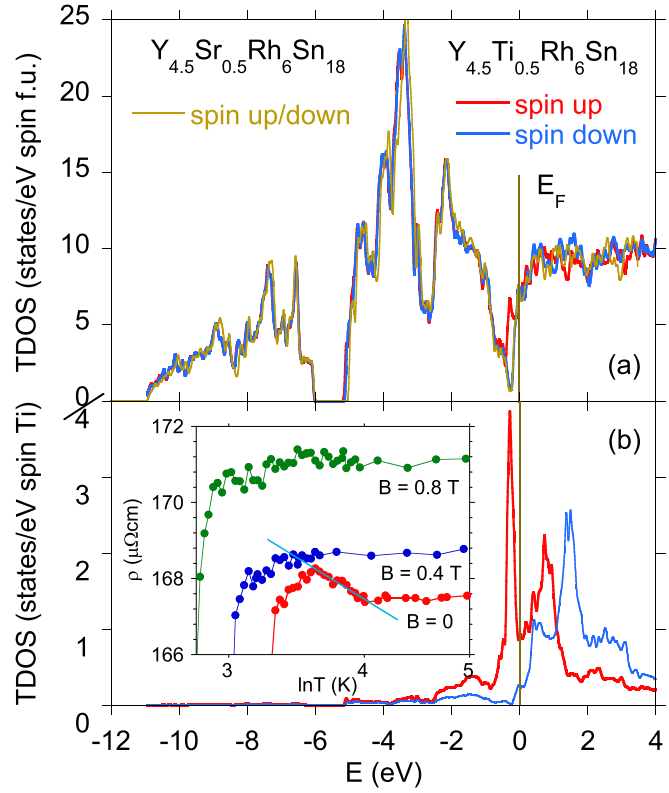


FIG. 21. (a) The total DOS per formula unit within GGA approximation (SO; $U_d = 3$ eV) for the both spin orientations (spin-up and spin-down) for $Y_{4.5}Ti_{0.5}Rh_6Sn_{18}$ and $Y_{4.5}Sr_{0.5}Rh_6Sn_{18}$. Panel (b) shows the spin-polarized TDOS for Ti per one Ti atom. The inset displays resistivity $\rho$ as a function of $lnT$ at various magnetic fields near $T_c$ for $Y_{4.5}Ti_{0.5}Rh_6Sn_{18}$.

is metallic, as shown in Fig. 9. Therefore, an interpretation based on stresses caused by $M$ dopants smaller than Y atoms seems more likely.

### E. Band structure of $Y_{4.5}M_{0.5}Rh_6Sn_{18}$

Figure 20 shows the valence band XPS spectra of $Y_{4.5}M_{0.5}Rh_6Sn_{18}$ in relation to the TDOS calculated for $Y_5Rh_6Sn_{18}$. All the VB XPS spectra are dominated by the Rh $4d$ and Sn $5p$ states between $\epsilon_F$ and $-5$ eV, while for binding energies $-3$ to $-11$ eV the Sn $5s$ states also give significant contribution to the intensity of these VB XPS spectra. For $Y_{4.5}Lu_{0.5}Rh_6Sn_{18}$, the Lu $4f$-electron states located at the binding energies $-7.7$ eV and $-9.1$ eV dominate the XPS VB spectra of this sample. We observed that the presence of $d$-electron states of metal $M$ did not significantly change the XPS spectra of $Y_5Rh_6Sn_{18}$, especially near the Fermi level, which is reflected in similar $T_c$ values measured for the series of $Y_{4.5}M_{0.5}Rh_6Sn_{18}$ superconductors.

As an example, the total DOS calculated for $Y_{4.5}Ti_{0.5}Rh_6Sn_{18}$ and $Y_{4.5}Sr_{0.5}Rh_6Sn_{18}$, assuming the correlation energy $U_d = 3$ eV only for Rh $4d$ states, is shown in Fig. 21. The DFT calculations were performed for only a single specific configuration of Ti (Sr) atoms in the Y sublattice. We are aware that to gain the complete knowledge of the effect of the dopants $M$ on the TDOS all symmetrically nonequivalent configurations should be considered in DFT calculations.

Assuming, that the configuration adopted for the calculations well reflects the real TDOS of $Y_{4.5}M_{0.5}Rh_6Sn_{18}$, then the most important results are following: (i) The atoms surrounding Ti move toward Ti [64], while the local distances between Sr neighbors increased in relation to the undoped compound $Y_5Rh_6Sn_{18}$ (see the data in Table III). This is the basis for PE modeling in Sec. IV. (ii) The Ti $d$-electron states form a sharp peak in the TDOS of $Y_{4.5}Ti_{0.5}Rh_6Sn_{18}$ at $\sim$0.3 eV below the Fermi level, thus removing the pseudogap, characteristic of the series of the remaining $Y_{4.5}M_{0.5}Rh_6Sn_{18}$ compounds [cf. Figs. 20 and 21(a)]. As a result, the resistivity of $Y_{4.5}Ti_{0.5}Rh_6Sn_{18}$ is metallic (cf. Fig. 9). (iii) The calculated Sommerfeld coefficient $\gamma_0$ is 34.7 mJ/mol K$^2$ for the Ti sample and 33.4 mJ/mol K$^2$ for the Sr one; both calculated quantities are quite comparable with those experimentally obtained from the specific heat data (cf. Table II). (iv) The *ab initio* calculations documented for the series of $Y_{4.5}M_{0.5}Rh_6Sn_{18}$ superconductors a nonmagnetic ground state, however, with the exception of the Ti dopant. The Ti dopant is calculated magnetic with the magnetic moment $\mu_{Ti} = 1.42\ \mu_B$ per atom, while the remaining dopants $M$ are calculated nonmagnetic. However, the experiment does not confirm the possible magnetic ground state for $Y_{4.5}Ti_{0.5}Rh_6Sn_{18}$; we therefore suggest a Kondo-impurity effect. One notes that the Ti dopant is only 1.7% of the total number of atoms in a unit cell, and the distance between the nearest Ti atoms is so large that the RKKY interaction between them is negligible. The inset to Fig. 21 exhibits a linear change in $\rho$ vs $\ln T$ between 3.5 K and 4 K, that is not observed in the applied magnetic fields. These temper-

TABLE III. Interatomic distances $d_Y$, $d_{Ti}$, $d_{Sr}$ (in Å) between the Y, Ti, Sr atom and atoms surrounding them in the relaxed crystal structure of $Y_5Rh_6Sn_{18}$ (third column), $Y_{4.5}Ti_{0.5}Rh_6Sn_{18}$ (fourth column), and $Y_{4.5}Ti_{0.5}Rh_6Sn_{18}$ (fifth column). For each composition the atomic relaxation (minimization of interatomic forces) was performed assuming the experimental lattice parameters. Multiplicity parameter (Mult.) gives the number of atoms of a given type in the local neighborhood of Y, Ti, and Sr atoms.

| Atom | Mult. | $Y_5Rh_6Sn_{18}$ $d_Y$ | $Y_{4.5}Ti_{0.5}Rh_6Sn_{18}$ $d_{Ti}$ | $Y_{4.5}Ti_{0.5}Rh_6Sn_{18}$ $d_{Sr}$ |
|---|---|---|---|---|
| Sn | 2 | 3.382 | 3.290 | 3.394 |
| Sn | 4 | 3.388 | 3.312 | 3.408 |
| Sn | 4 | 3.403 | 3.322 | 3.421 |
| Sn | 2 | 3.423 | 3.351 | 3.438 |
| Rh | 2 | 3.508 | 3.509 | 3.534 |
| Rh | 4 | 3.515 | 3.543 | 3.546 |

ature and field dependencies of $\rho$ are characteristic of the Kondo-impurity behavior. Similarly, a broad maximum in the $C(T)/T$ data above $T_c^\star$ shown in Fig. 6 may also indicate a Kondo effect coexisting with the distribution of $\Delta$'s in the region of the inhomogeneous superconducting phase; however, both of these effects are difficult to be separated exactly.

## IV. TOY MODEL

We propose a simple model to verify whether the observed PE described in the previous section can be caused by the local dopant-induced changes in the crystal lattice geometry. It has been widely accepted that this effect results from a change in the structure of the vortex lattice close to $H_{c2}$ or $T_c$. At low temperature, the vortex lines form a regular lattice. When the temperature approaches $T_c$ the flux line lattice starts to melt, which allows individual flux lines to deviate from an ideal periodic lattice and go through pinning centers. That means that the presence of the PE should be correlated with the effectiveness of the pinning of flux lines. And since we observe the PE only when Y atoms are replaced by smaller atoms, we want to check how the size of the impurity affects the pinning energy. The pinning energy $E_p$ is defined as the energy that is gained when the vortex core is located at the impurity site [65],

$$E_p = E(r = 0) - E(r = \infty), \tag{10}$$

where $E(r)$ is the energy of the system when the distance between the impurity site and the vortex core is $r$. Since both the size of the area affected by the impurity and the vortex size are limited, for $r \to \infty$ the energy of the vortex is not affected by the impurity and we can divide the system into two parts: one with the impurity and one homogeneous. Then, we independently calculate the energy of both parts with and without the vortex (see Fig. 22). The total energy (for $r = 0$ and for $r = \infty$) is a sum of these energies.

What is interesting for our analysis is the dependence of the pinning energy on the impurity size. In particular, we want to determine whether the strength of the pinning depends on whether the impurity is smaller or larger than Y atoms. The lattice deformations for small and large impurities are schematically demonstrated in Fig. 23. It has already been discussed that impurities smaller then Y atoms lead to a small decrease in the total volume of the sample. The most pronounced effects on the crystal lattice are, however, in the vicinity of the impurity site. In Fig. 23 we marked this region by a light gray circle and assume that the changes are negligible beyond this area. For an impurity larger than Y atoms, the lattice is locally compressed so that the length of the bonds is reduced near the impurity. In contrast, for a small impurity the length increases.

To calculate $E_p$ for a given impurity size we model the system by a tight-binding 2D lattice with hopping integral $t_{ij}$ between nearest neighbor sites $i$ and $j$ given by

$$t_{ij} = t_0(1 + ae^{-br}), \tag{11}$$

where $r$ is the distance between the center of bond $i$-$j$ and the impurity site. Parameter $a$ is assumed so that the $t_{ij}$ significantly differs from $t_0$ only within a few lattice constants from the impurity site. Parameter $a$ describes the magnitude of the lattice constant changes and additionally $a > 0$ ($t_{ij} > t_0$) for impurities larger than Y atoms and $a < 0$ ($t_{ij} < t_0$) for impurities smaller than Y atoms.

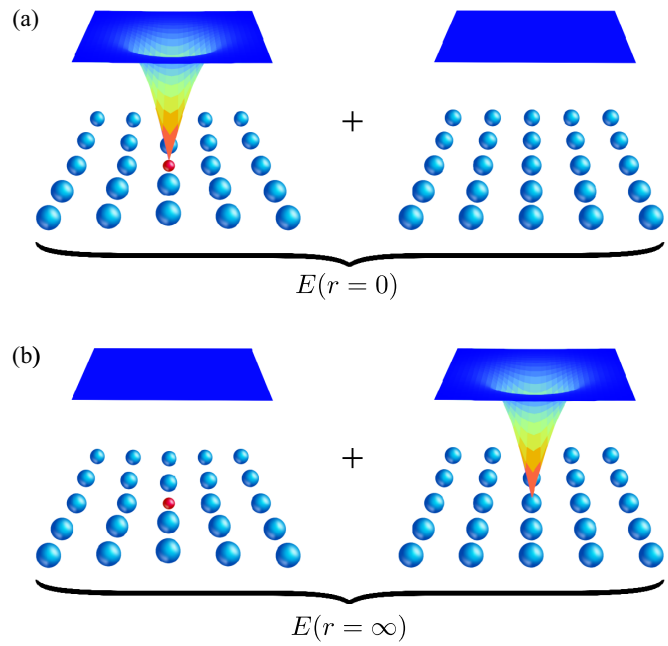


FIG. 22. Illustration of the vortex configurations used to calculate the pinning energy according to Eq. (10). Panel (a) shows the situation when the vortex is pinned at the impurity (represented by a small red sphere; $r = 0$), whereas in panel (b) the vortex is located away from the impurity ($r = \infty$).

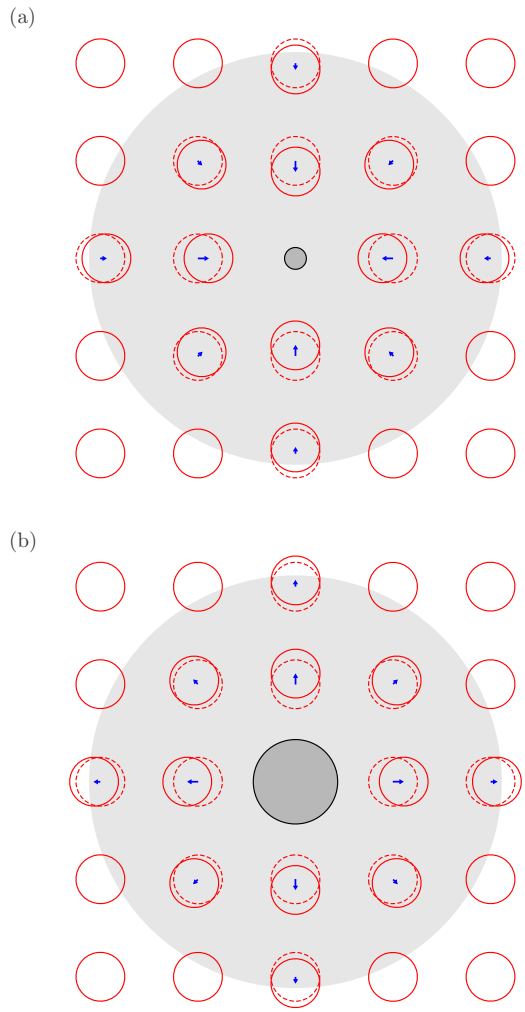


FIG. 23. Schematic illustration of local atom displacements around an impurity smaller (a) and larger (b) than Y atoms (not to scale). The dashed circles represent a perfect square lattice without the impurity-induced distortion. The light gray shaded area shows the range of the influence of the impurity.

We assume $s$-wave pairing, so the model Hamiltonian can be written as

$$H = \sum_{ij\sigma} t_{ij} e^{i\phi_{ij}} c^{\dagger}_{j\sigma} c_{i\sigma} - \mu \sum_{i\sigma} n_{i\sigma} - \sum_{i} (\Delta_i c^{\dagger}_{i\uparrow} c^{\dagger}_{i\downarrow} + \text{H.c.}) + V_{\text{imp}} n_k, \tag{12}$$

where $t_{ij}$ is given by Eq. (11), $n_{i\sigma} = c^{\dagger}_{i\sigma} c_{i\sigma}$, $n_k = n_{k\uparrow} + n_{k\downarrow}$, $\mu$ is the chemical potential, and the impurity has potential $V_{\text{imp}}$ and is located at lattice site $k$. In the mixed state, the magnetic field effect is included through the Peierls phase factor [66]

$$t_{ij} \to t_{ij} e^{i\phi_{ij}}, \tag{13}$$

where

$$\phi_{ij} = \frac{e}{\hbar} \int_{\boldsymbol{r}_j}^{\boldsymbol{r}_i} \boldsymbol{A}(\boldsymbol{r}) d\boldsymbol{r}. \tag{14}$$

The mean-field pair potential $\Delta_i$ is defined as

$$\Delta_i = V_s \langle c_{i\downarrow} c_{i\uparrow} \rangle, \tag{15}$$

where $V_s > 0$ is the on-site attractive potential leading to the pairing in the $s$-wave channel and $\langle \ldots \rangle$ denotes the thermodynamic average. Hamiltonian (12) can be diagonalized with the help of the Bogoliubov–de Gennes (BdG) equations [67]. We introduce a set of new fermionic operators $\gamma^{(\dagger)}_{n\sigma}$:

$$c_{i\uparrow} = \sum_l u_{il} \gamma_{l\uparrow} - v^{*}_{il} \gamma^{\dagger}_{l\downarrow}, \tag{16}$$

$$c_{i\downarrow} = \sum_l u_{il} \gamma_{l\downarrow} + v^{*}_{il} \gamma^{\dagger}_{l\uparrow}, \tag{17}$$

where $u_{il}$ and $v_{il}$ are solutions of

$$\sum_j \begin{pmatrix} \mathcal{H}_{ij} & \mathcal{D}_{ij} \\ \mathcal{D}^{*}_{ij} & -\mathcal{H}_{ij} \end{pmatrix} \begin{pmatrix} u_{jl} \\ v_{jl} \end{pmatrix} = E_l \begin{pmatrix} u_{jl} \\ v_{jl} \end{pmatrix}. \tag{18}$$

Here, $\mathcal{H}_{ij} = t_{ij} e^{i\phi_{ij}} - \mu \delta_{ij}$ and $\mathcal{D}_{ij} = \Delta_i \delta_{ij}$. The order parameter $\Delta_i$ is calculated self-consistently,

$$\Delta_i = V_s \sum_l u_{il} v^{*}_{il} \tanh\left(\frac{E_l}{2k_{\text{B}}T}\right). \tag{19}$$

## Results

To determine the pinning energy, we need to calculate $E(r = 0)$ and $E(r = \infty)$ [see Eq. (10)]. To do that, we consider two $35 \times 35$ lattices: one with uniformly placed lattice sites and one with lattice sites shifted by the presence of an impurity (toward the impurity site or away from it; see Fig. 23). For both these systems, the BdG equations are solved iteratively, but the initial configuration of $\Delta_i$ in one of the systems is such that its phase changes by $2\pi$ when encircling the center of the system. This is the system where the vortex is located. Its profile is self-consistently determined by solving the BdG equations. Since even in the absence of a vortex the order parameter $\Delta_i$ can be affected by the impurity-induced dislocations, we also need to solve the BdG equations for the other system.

Then, $E(r = 0)$ is defined as the total energy of both the systems calculated for the vortex located in the system with the impurity. Similarly, $E(r = \infty)$ is the total energy in the case where the vortex is located in the system without an impurity (see Fig. 22). The energy of each of them is calculated as

$$E^{(k)} = \sum_l E^{(k)}_l \sum_i \left\{ \left|u^{(k)}_{il}\right|^2 f\left(E^{(k)}_l\right) + \left|v^{(k)}_{il}\right|^2 \left[1 - f\left(E^{(k)}_l\right)\right] \right\}, \tag{20}$$

where $f(\ldots)$ is the Fermi-Dirac distribution function and $k = 1, 2$ enumerates the systems with and without an impurity. The total energy is $E = E^{(1)} + E^{(2)}$. Since we want to analyze the influence of the displacements of atoms around an impurity, we assume that $V_{\text{imp}}$ does not change with the size of the impurity so that $E_p$ describes only the contribution to the pinning energy from the lattice distortion.

Figure 24 shows the resulting pinning energy (10) as a function of parameter $a$ [see Eq. (11)]. It can be seen there that arbitrary deformation produced by an impurity leads to vortex

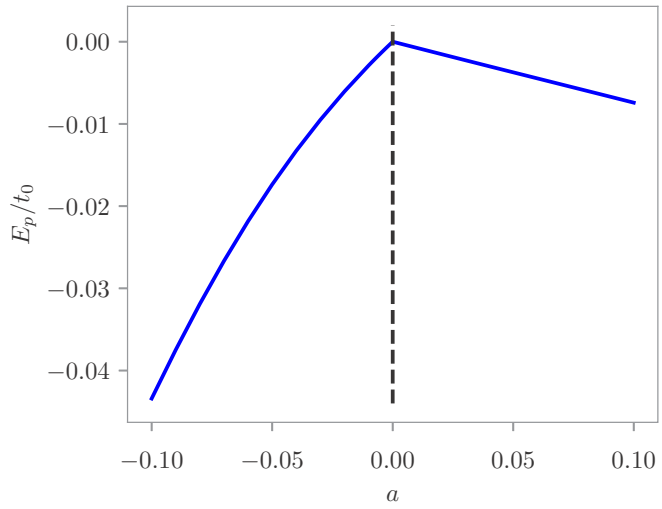


FIG. 24. The pinning energy [Eq. (10)] as a function of parameter $a$. $a < 0$ ($a > 0$) corresponds to impurities smaller (larger) than Y atoms. The dashed line shows $a = 0$, i.e., a situation when there is no impurity-induced deformation.

pinning (or enhances pinning if the impurity itself is a pinning center). Note, however, that for $a < 0$, which corresponds to an impurity smaller than Y atoms, the pinning is significantly stronger. This is one of the possible explanations why the PE is seen only when Y is substituted by smaller atoms. It also suggests that this effect may be observed if Rh is substituted by smaller atoms, which will be verified in future studies.

## V. CONCLUDING REMARKS

In summary, we performed comprehensive investigations of the polycrystalline $Y_{4.5}M_{0.5}Rh_6Sn_{18}$ samples and confirmed that their superconducting transition temperature $T_c$ increases with the random disorder. These disordered samples exhibit coexistence between a bulk superconducting phase and a higher-$T_c$, inhomogeneous superconducting phase. Evidence is provided that the degree of local chemical disorder, characterized by the difference between the electron-phonon coupling parameters for the two superconducting phases, $\Delta\lambda$, correlates with the emergence of the higher-$T_c$ state. The observed phenomenon can be understood within the Gasti-asoro and Andersen theoretical approach [20]. In a series of our previous reports, we proposed a phenomenological model to explain the enhanced superconductivity of the family of similar skutterudite-related superconductors by different stiffness of the bulk ($T_c$) and inhomogeneous ($T_c^\star$) phases. The enhancement of $T_c$ here is related to stemming from two effects. One is an inhomogeneous SC $T_c^\star$ phase due to an inhomogeneous doping effect, which appears to be closer to a pressure effect; the second is a peak effect, which is not an enhancement of $T_c$, but mainly an enhancement of the critical current. Here, we have demonstrated that the field-induced reentrant superconductivity and the peak effect are observed when the atomic radius of metal $M$ is smaller than the radius for Y (i.e., $M =$ Zr, Ti, Lu, vacancies). The effect is not observed when the atomic radius of $M$ is greater than that of Y. We hypothesize that this reentrant superconductivity and its associated peak effect are consequences of variations in the structure of the vortex lattice under applied fields near the critical field $H_{c2}$. Reentrant superconductivity and the peak effect are also more prominent in samples with larger values of $\Delta\lambda$. The PE was also documented for the $Lu_{5-\delta}Rh_6Sn_{18}$ sample with vacancies in Lu sites [68]. Therefore, one can assume that the anomalous reentrance of superconductivity in the defected quasiskutterudites results from the stress located on the local defects. We also proposed a simple theoretical model which demonstrated that the lattice distortion produced by an impurity smaller then Y leads to stronger pinning than that produced by a larger impurity. A toy model is presented in which the dependence of the pinning energy, $E_p$, on the size of impurities is computed. These calculations show the pinning is much stronger when the atomic radius of $M$ is smaller than that of Y. The resulting impact on flux lattice dynamics is responsible for the reentrant superconductivity and associated peak effect in samples with $M =$ Zr, Ti, Lu vacancies.

## ACKNOWLEDGMENTS

We are grateful to Krzysztof Rogacki for fruitful discussions. M.M.M. acknowledges support by the National Science Centre (Poland) under Grant No. DEC-2018/29/B/ST3/01892.

[1] A. F. Hebard and M. A. Paalanen, Phys. Rev. B **30**, 4063 (1984).
[2] D. B. Haviland, Y. Liu, and A. M. Goldman, Phys. Rev. Lett. **62**, 2180 (1989).
[3] H. Alloul, J. Bobroff, M. Gabay, and P. J. Hirschfeld, Rev. Mod. Phys. **81**, 45 (2009).
[4] A. A. Abrikosov and L. P. Gor'kov, Zh. Eksp. Teor. Fiz. **39**, 1781 (1961) [Sov. Phys. JETP **12**, 1243 (1961)].
[5] Y.-J. Kim and A. W. Overhauser, Phys. Rev. B **47**, 8025 (1993).
[6] P. W. Anderson, J. Phys. Chem. Solids **11**, 26 (1959).
[7] A. A. Golubov and I. I. Mazin, Phys. Rev. B **55**, 15146 (1997).
[8] M. B. Maple, P.-C. Ho, V. S. Zapf, N. A. Frederick, E. D. Bauer, W. M. Yuhasz, F. M. Woodward, and J. W. Lynn, J. Phys. Soc. Jpn. Suppl. **71**, 23 (2002).
[9] R. Vollmer, A. Faißt, C. Pfleiderer, H. v. Löhneysen, E. D. Bauer, P.-C. Ho, V. Zapf, and M. B. Maple, Phys. Rev. Lett. **90**, 057001 (2003).
[10] G. Seyfarth, J. P. Brison, M.-A. Méasson, D. Braithwaite, G. Lapertot, and J. Flouquet, Phys. Rev. Lett. **97**, 236403 (2006).
[11] M. E. McBriarty, P. Kumar, G. R. Stewart, and B. Andraka, J. Phys.: Condens. Matter **21**, 385701 (2009).
[12] M.-A. Méasson, D. Braithwaite, G. Lapertot, J.-P. Brison, J. Flouquet, P. Bordet, H. Sugawara, and P. C. Canfield, Phys. Rev. B **77**, 134517 (2008).
[13] A. Bianchi, R. Movshovich, M. Jaime, J. D. Thompson, P. G. Pagliuso, and J. L. Sarrao, Phys. Rev. B **64**, 220504(R) (2001).

[14] J. S. Kim, D. J. Mixson, D. J. Burnette, T. Jones, P. Kumar, B. Andraka, G. R. Stewart, V. Craciun, W. Acree, H. Q. Yuan, D. Vandervelde, and M. B. Salamon, Phys. Rev. B **71**, 212505 (2005).

[15] T. Cren, D. Roditchev, W. Sacks, J. Klein, J.-B. Moussy, C. Deville-Cavellin, and M. Laguës, Phys. Rev. Lett. **84**, 147 (2000).

[16] B. M. Andersen, A. Melikyan, T. S. Nunner, and P. J. Hirschfeld, Phys. Rev. B **74**, 060501(R) (2006).

[17] B. Liu, J. Wu, Y. Cui, H. Wang, Y. Liu, Z. Wang, Z. Ren, and G. Cao, Supercond. Sci. Technol. **31**, 125011 (2018).

[18] J. Peng, Z. Yu, J. Wu, Y. Zhou, Y. Guo, Z. Li, J. Zhao, Ch. Wu, and Y. Xie, ACS Nano **12**, 9461 (2018).

[19] A. Ślebarski and M. M. Maśka, Materials **13**, 5830 (2020).

[20] M. N. Gastiasoro and B. M. Andersen, Phys. Rev. B **98**, 184510 (2018).

[21] M. A. R. LeBlanc and W. A. Little, in *Proceedings of the VII International Conference on Low Temperature Physics, 1960* (University of Toronto Press, Toronto, 1960), p. 198.

[22] P. L. Gammel, U. Yaron, A. P. Ramirez, D. J. Bishop, A. M. Chang, R. Ruel, L. N. Pfeiffer, E. Bucher, G. D'Anna, D. A. Huse, K. Mortensen, M. R. Eskildsen, and P. H. Kes, Phys. Rev. Lett. **80**, 833 (1998).

[23] M. Isino, T. Kobayashi, N. Toyota, T. Fukase, and Y. Muto, Phys. Rev. B **38**, 4457 (1988).

[24] A. D. Huxley, C. Paulsen, O. Laborde, J. L. Tholence, D. Sanchez, A. Junod, and R. Calemczuk, J. Phys.: Condens. Matter **5**, 7709 (1993); S. B. Roy and P. Chaddah, *ibid.* **9**, L625 (1997).

[25] H. Sato, Y. Akoi, H. Sugawara, and T. Fukahara, J. Phys. Soc. Jpn. **64**, 3175 (1995).

[26] S. Sarkar, D. Pal, S. S. Banerjee, S. Ramakrishnan, A. K. Grover, C. V. Tomy, G. Ravikumar, P. K. Mishra, V. C. Sahni, G. Balakrishnan, D. McK. Paul, and S. Bhattacharya, Phys. Rev. B **61**, 12394 (2000).

[27] R. Modler, P. Gegenwart, M. Lang, M. Deppe, M. Weiden, T. Luhmann, C. Geibel, F. Steglich, C. Paulsen, J. L. Tholence, N. Sato, T. Komatsubara, Y. Onuki, M. Tachiki, and S. Takahashi, Phys. Rev. Lett. **76**, 1292 (1996).

[28] M. Tachiki, S. Takahashi, P. Gegenwart, M. Weiden, M. Lang, C. Geibel, F. Steglich, R. Modler, C. Paulsen, and Y. Onuki, Z. Phys. B: Condens. Matter **100**, 369 (1996).

[29] X. Ling and J. I. Budnick, in *Magnetic Susceptibility of Superconductors and Other Spin Systems*, edited by R. A. Hein, T. L. Francavilla, and D. H. Liebenberg (Plenum Press, New York, 1991), p. 377.

[30] W. K. Kwok, J. A. Fendrich, C. J. van der Beek, and G. W. Crabtree, Phys. Rev. Lett. **73**, 2614 (1994).

[31] A. B. Pippard, Philos. Mag. **19**, 217 (1969); A. M. Campbell and J. E. Evetts, Adv. Phys. **21**, 327 (1972).

[32] P. Fulde and R. A. Ferrell, Phys. Rev. **135**, A550 (1964).

[33] A. I. Larkin and Y. N. Ovchinnikov, Zh. Eksp. Teor. Fiz. **47**, 1136 (1964) [Sov. Phys. JETP **20**, 762 (1965)].

[34] S. Miraglia, J. L. Hodeau, F. Bergevin, and M. Marezio, Acta Cryst. Sect. B **43**, 76 (1987).

[35] J. L. Hodeau, M. Marezio, and J. P. Remeika, Acta Cryst. B **40**, 26 (1984).

[36] J. Rodriguez-Carvajal, Phys. B: Condens. Matter **192**, 55 (1993).

[37] D. J. Singh and L. Nordstrom, *Plane Waves, Pseudopotentials, and the LAPW Method*, 2nd ed. (Springer Science, 2006).

[38] P. Blaha, K. Schwarz, G. K. H. Madsen, D. Kvasnicka, J. Luitz, R. Laskowski, F. Tran, and L. D. Marks, *WIEN2k, An Augmented Plane Wave + Local Orbitals Program for Calculating Crystal Properties* (Karlheinz Schwarz, Technische Universität Wien, Austria, 2001).

[39] J. P. Perdew, A. Ruzsinszky, G. I. Csonka, O. A. Vydrov, G. E. Scuseria, L. A. Constantin, X. Zhou, and K. Burke, Phys. Rev. Lett. **100**, 136406 (2008).

[40] V. I. Anisimov, J. Zaanen, and O. K. Andersen, Phys. Rev. B **44**, 943 (1991).

[41] A. Ślebarski, P. Zajdel, M. M. Maśka, J. Deniszczyk, and M. Fijałkowski, J. Alloys Compd. **819**, 152959 (2020).

[42] A. Ślebarski, M. Fijałkowski, M. M. Maśka, J. Deniszczyk, P. Zajdel, B. Trump, and A. Yakovenko, Phys. Rev. B **103**, 155133 (2021).

[43] B. H. Toby, Powder Diffr. **21**, 67 (2006).

[44] A. Ślebarski, M. Fijałkowski, M. M. Maśka, M. Mierzejewski, B. D. White, and M. B. Maple, Phys. Rev. B **89**, 125111 (2014).

[45] In the case of strongly disordered quasiskutterudites with $T_c \approx T_c^\star$, like $La_3(CoRu_3)Sn_{13}$ [46], the specific heat of the sample shows only a broad and poorly visible maximum around $T_c^\star$, well described by the function $f(\Delta)$.

[46] A. Ślebarski, M. M. Maśka, M. Fijałkowski, C. A. McElroy, and M. B. Maple, J. Alloys Compd. **646**, 866 (2015).

[47] B. Zeimetz, B. Glowacki, and J. Evetts, Eur. Phys. J. B **29**, 359 (2002).

[48] D. Bucheli, S. Caprara, C. Castellani, and M. Grilli, New J. Phys. **15**, 023014 (2013).

[49] T. P. Orlando, E. J. McNiff, Jr., S. Foner, and M. R. Beasley, Phys. Rev. B **19**, 4545 (1979).

[50] E. Helfand and N. R. Werthamer, Phys. Rev. Lett. **13**, 686 (1964); N. R. Werthamer, E. Helfand, and P. C. Hohenberg, Phys. Rev. **147**, 295 (1966).

[51] P. E. Seiden, Phys. Rev. **179**, 458 (1969).

[52] P. Morel and P. W. Anderson, Phys. Rev. **125**, 1263 (1962).

[53] W. L. McMillan, Phys. Rev. **167**, 331 (1968).

[54] J. J. Hopfield, Phys. Rev. **186**, 443 (1969).

[55] For $Y_{4.5}La_{0.5}Rh_6Sn_{18}$, there was no deficiency of Y (Table I). Its pseudogap in the total DOS is expected about 0.3 eV below the Fermi level, and results the metallic behavior of the sample. The Ti $d$-electron states for $Y_{4.5}Ti_{0.5}Rh_6Sn_{18}$ are located at $\epsilon_F$ (see Fig. 21, and also Ref. [56]), which could explain the metallic character of $\rho$.

[56] H. Höchst, P. Steiner, G. Reiter, and S. Hüfner, Z. Phys. B **42**, 199 (1981).

[57] N. F. Mott, *Metal-Insulator Transitions* (Taylor and Francis, London, 1974).

[58] N. F. Mott, Philos. Mag. **13**, 989 (1966).

[59] M. Gamża, W. Schnelle, A. Ślebarski, U. Burkhardt, R. Gumeniuk, and H. Rosner, J. Phys.: Condens. Matter **20**, 395208 (2008).

[60] A. Ślebarski, J. Goraus, and P. Witas, Phys. Rev. B **92**, 155136 (2015).

[61] J. Spałek, A. Ślebarski, J. Goraus, L. Spałek, K. Tomala, A. Zarzycki, and A. Hackemer, Phys. Rev. B **72**, 155112 (2005).

[62] A detailed analysis of the characteristics of $\rho_T(B)$ for the $Lu_{5-\delta}Rh_6Sn_{18}$ sample also shows a very weak peak effect, due to the presence of small number of vacancies in the Lu sites, but the effect is weak and comparable with measurement noise.

[63] A. Ślebarski, J. Goraus, P. Witas, L. Kalinowski, and M. Fijałkowski, Phys. Rev. B **91**, 035101 (2015).

[64] An atomic relaxation was performed in DFT calculations to reach the equilibrium structure.

[65] Q. Han, L.-y. Zhang, and Z. D. Wang, Phys. Rev. B **62**, 5936 (2000).

[66] R. E. Peierls, Z. Phys. **80**, 763 (1933); J. M. Luttinger, Phys. Rev. **84**, 814 (1951).

[67] P.-G. de Gennes, *Superconductivity of Metals and Alloys* (W. A. Benjamin, New York, 1966).

[68] Unfortunately, we could not demonstrate the PE generated by the Y vacancies, because we were unable to obtain the off-stoichiometric $Y_{4.5}Rh_6Sn_{18}$ sample.